Guidance, Navigation, and Control System for Landing near Plume Source on Enceladus

Kostas Konstantinidis* and Roger Förstner†
Bundeswehr University Munich, 85579 Neubiberg, Germany

https://doi.org/10.2514/1.G004760

Saturn's moon Enceladus is one of the most promising candidates in the solar system for hosting microbial life. Plumes emanating from its south pole are ejecting water directly from the ocean to space. The Enceladus Explorer (EnEx) lander mission concept aims to land near a plume source and deploy a melting probe to sample liquid pockets under the plumes for life. Landing there would be exceptionally challenging due to the rough canyonous topography, polar lighting conditions, a surface covered by superfine snow, and strict planetary protection regulations. In this work the Guidance, Navigation, and Control (GN&C) system and operations for the critical approach phase of such a landing are investigated. An advanced GN&C system is defined, comprising extended Kalman filter simultaneous localization and mapping (EKF-SLAM)–based navigation, fuzzy-reasoning-based hazard detection and avoidance, and convex guidance. To verify the landing feasibility and further refine the concept, the system is investigated using a closed-loop simulation tool we created. The performance of each function is analyzed separately with sensitivity and worst-case analyses. A Monte Carlo simulation encompassing all functions is performed to estimate mission success statistics.

I. Introduction

THE search for life in the solar system has been one of the main driving forces behind space exploration. The recent discoveries that the icy moons of the giant planets in our solar system contain vast oceans have made them prime targets for that search. In particular, Saturn's moon Enceladus is one of the most promising candidates among the icy moons and appears to fulfill the basic habitability requirements [1–3].

Plume jets found to emanate from the south pole of Enceladus by the recently decommissioned Cassini spacecraft further point to a chemically rich ocean hospitable to microbial life [4]. They offer in addition a rare opportunity for the in situ sampling of ocean material, as microbes from the ocean could be carried along with the ocean water, and then ejected to space via the plumes [5]. The microbes would remain in their unaffected state up to a certain depth under the plumes and could even form small microbial communities in pockets of liquid water close to the plume channel and near the surface [5]. The combination of the relative ease of access to these water pockets and the freshness of the material contained in them makes them a very desirable target for in situ astrobiology.

A mission concept for the in situ astrobiological sampling of a relatively shallow water pocket (∼200 m) under a plume source on Saturn's moon Enceladus was developed between 2012 and 2015 at the Institute of Space Technology & Space Applications (ISTA) of Bundeswehr University Munich. The lander would land near a plume source and deploy a future version of the IceMole melting probe currently under development by FH Aachen [6]. That work was part of the joint research collaboration of eight German universities called Enceladus Explorer (EnEx) and funded by the German Space Administration (DLR). A detailed mission concept for the EnEx Lander is given in [7].

An important part of the EnEx Lander concept is a safe and accurate planetary landing. The final approach phase in particular emerges as a critical and complex operational phase: in a span of a few minutes the landing guidance, navigation, and control (GN&C) system must apply the full extent of its capabilities to ensure a safe and accurate landing. A detailed closer look into the approach phase, and an extended effort into designing the needed system and operations would be central in furthering the development of the EnEx Lander concept.

The goal of this paper is therefore to investigate the approach phase of a safe and accurate landing near a plume source on the bottom of a tiger stripe canyon on Enceladus.

Past robotic planetary landings have been automated, landing blindly while following either a timed preset event sequence or using simple triggers, such as a certain altitude reached. Of the currently planned missions, NASA's Mars 2020 will navigate by comparing camera images to an a priori map stored onboard, and performing simple avoidance maneuvers to premarked hazardous areas known to exist on that a priori map [8]. Several novel landing mission concepts similar to the EnEx Lander exist (ESA Lunar Lander [9,10], NASA's Lunar MARE [8,11]) as well as technology development efforts for advanced landing GN&C (NASA's ALHAT and COBALT [8,12], PILOT by ESA and Airbus [13]). No detailed, dedicated GN&C system has been proposed for landing on the icy moons, except in terms of potential and partial reuse of technologies used, e.g., for lunar landing as seen above.

Enceladus is a small icy moon (diameter ∼500 km) orbiting Saturn at a radius of 4 Saturn radii, with an approximate surface gravity of 0.113 m/s^2 [14,15]. More details on Enceladus are given in [14,15]. The relevant environmental details for the EnEx Lander are given in detail in [7,16] but will be summarized here for convenience.

Local topography: Around 100 plume sources are interspersed along the canyon bottoms of the South-Polar Terrain (SPT) of Enceladus [5]. Each canyon ridge is about 100–150 m high, whereas the valley is about 200–250 m deep and 50–100 m wide at the bottom. The canyon faces have a maximum slope of ∼30° [17] (Fig. 1).

Terrain texture: The SPT is covered in plume fallout with a thickness up to tens of meters [18]. Still, exposed icy crust can also be encountered, especially on slopes. The mechanical behavior of this plume fallout or "snow" is very uncertain. It could act as very fine dust or even like dry quicksand [19], or thermal cycling could have caused fallout particles to sinter, resulting in a hard surface.

Illumination conditions: The SPT is characterized by polar illumination conditions with each season lasting approximately 8 years.‡ The maximum sun elevation during summer solstice does not exceed 40°.

Received 15 August 2019; revision received 15 June 2020; accepted for publication 29 July 2020; published online 22 September 2020.

*Research Assistant, Institute for Space Technology and Space Applications, Department of Aerospace Engineering; currently Internal Research Fellow, Advanced Concepts Team (ACT), European Space Research and Technology Centre (ESTEC), European Space Agency (ESA), Keplerlaan 1, 2201 AZ Noordwijk, The Netherlands.

†Professor, Institute for Space Technology and Space Applications, Department of Aerospace Engineering.

‡The next Saturnian southern summer period will begin in the year 2028 and last until beginning of 2036 with the peak in 2032.

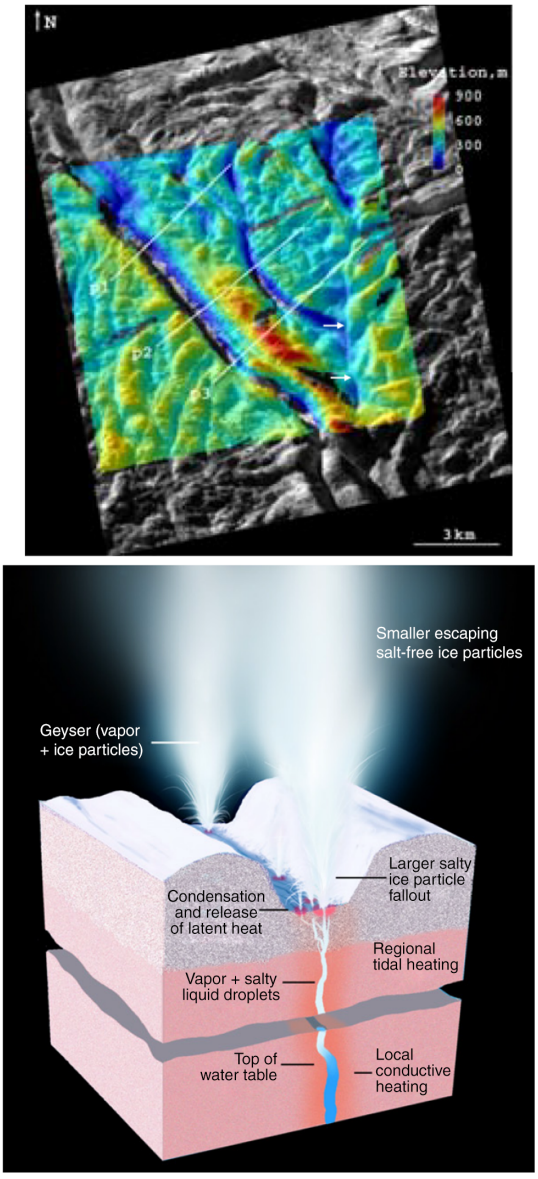

Fig. 1 Above: Stereo-derived elevation model of characteristic canyon area on the SPT [17]. Below: Small-scale physical and thermal structure and processes relevant to Enceladus's geysering activity [5].

Thermal environment: The plume sources act as concentrated hot spots reaching temperatures up to 200 K in concentrated areas (tens of meters) surrounding the plumes (Fig. 1) [5,20]. Because of the large difference in thermal inertias between super-fine snow and exposed ice in the canyons [21], the surface temperature is expected to vary significantly depending on local texture.

Plume "atmosphere": The density of H_2O molecules already a few meters away from the plume source mouths is negligible for engineering purposes. Equally negligible is the flow of ice particles spewed by the plumes, with larger particles only reaching small velocities and low altitudes [22].

Planetary protection (PP): The open plume channels on the SPT could lead directly downward into a liquid water environment. The PP sensitivity of such a mission would be thus unprecedented.

Radiation environment: Radiation in the vicinity of Enceladus is significantly less harsh than, e.g., that of Europa [15].

From the environmental, operational, and regulation aspects described in the previous sections, the requirements for landing near a plume source were deduced.[§] The landing must be accurate: the lander should land no further than 50 m from the plume source, based on the size of the canyon bottom and the limited length of the tether of the IceMole. The landing must also be safe, meaning that the landing site characteristics (e.g., roughness) should respect the tolerances of the lander. We also assumed that it would be preferable (but not an absolute requirement) to land on ice rather on snow. Finally the landing must be reliable. Planetary landings have reliability in the order of ∼99%, but due to planetary protection concerns an even higher reliability might be required. This analysis is left for the future. Also due to planetary concerns, the lander must not land too close to the plume source, e.g., further than 5 m.

Because of the uncertainties in orbital maps and imperfect lander navigation, it is practically impossible for an automated sequential landing with a precalculated trajectory to achieve the above requirements. It would be further impossible to remotely control the landing due to the ∼3 h two-way signal delay from Earth to Saturn. The functions necessary for a successful landing must be then performed autonomously onboard.

II. Autonomous Landing on Enceladus

The requirements derived above can be allocated to top-level functions of a landing GN&C system:

1) *Sensing* senses elements of the surrounding environment and of the lander itself.

2) *Navigation* estimates the navigational state of the lander.

3) *Hazard detection and avoidance (HDA)* identifies hazards and commands a retargeting to a new suitable landing spot if needed.

4) *Guidance* calculates a feasible trajectory from the current lander position to the selected landing target.

5) *Control* derives the commands necessary to match the current vehicle state with the desired path provided by the guidance function.[¶]

A 3-degree-of-freedom (3-DOF) model is applied for the following analysis, with the lander considered a point mass. This is a common assumption made in similar analyses, as the attitude control takes place in far higher frequencies than that of the translational control—the two can thus be considered separately [23]. Where necessary, the thrust pointing vector can be considered as a proxy for lander attitude.

The foundations for each of the top-level functions for landing GN&C for the EnEx Lander will be discussed and analyzed in the following.

A. Sensing

An Inertial Navigation System (INS) is used as the basis for navigation here, using its constituent accelerometer to measure the nongravitational accelerations acting on the carrying vehicle, and by double integration, to estimate successively the vehicle velocity and position. Some simplifications can be made concerning inertial navigation, in order to maintain a manageable scope for this holistic work. In particular, considering the small timescales involved in the approach phase landing problem studied here, only a small white noise will be taken into consideration as a measurement error.[**] For the same reason an ideally known gravity model is assumed, ignoring any gravity model uncertainties as given in [15].[††]

Two types of exteroceptive sensors were considered: cameras and lidar. An optical camera was used to sense the visible spectrum and a thermographic (or thermal) camera to sense the rich thermal environment of the SPT canyons. A flash lidar was used, with an important assumption attached: due to the differences in texture and reflectance between ice and snow, each lidar ray can sense the terrain texture by analyzing the return signal, although with a high degree of uncertainty (see, e.g., [25]).

[§]A detailed list of requirements and lander tolerances is given in [16].

[¶]Here focus is given to the other functions of GN&C, considered as higher level functions, and ideal control will be assumed.

**Back-of-the-envelope calculations showed that drifts introduced by accelerometer bias are within acceptable limits (submeter for position, and a few centimeter/second for velocity). In addition, as the navigation function here relies significantly on absolute measurements of the lander state (see the following section), these small drifts are anyway considered to be correctable by these absolute measurements [24].

[††]Initial simulations confirmed the negligible effect of gravity model uncertainties for approach phase landing operations.

B. Navigation

Traditional landing approaches based on inertial sensing only do not have the navigational precision to meet the high accuracy requirements. In addition, a mapping element must also be added for any sensed elements of the environment (plume source) to be localized relative to the lander. The problem then becomes one of simultaneous localization and mapping (SLAM). In this work, an extended Kalman filter is applied as the basis for a SLAM algorithm (EKF-SLAM) [26,27].

1. Simultaneous Localization and Mapping (EKF-SLAM)

In EKF-SLAM, the map vector is defined as a state vector containing the vehicle pose (position, velocity, etc.) and the currently mapped landmark positions. The map in EKF is modeled as a Gaussian variable using the mean and the covariance matrix of the state vector, denoted, respectively, by $\hat{\boldsymbol{x}}$ and $\boldsymbol{P}$.[‡‡]

The goal of EKF-SLAM is then to maintain the map $\{\hat{\boldsymbol{x}}, \boldsymbol{P}\}$ up-to-date when the vehicle moves (prediction), when it perceives a landmark it has already observed (observation–correction), and when it perceives a new landmark and decides to add it to the map (landmark perception and initialization). At each step of the EKF-SLAM process, the map vector and the covariance matrix are modified accordingly. A full mathematical description of the above process can be found in [16,26–28].

In the above process, a distinction between a priori known and unknown landmarks is made. If an observed landmark is considered a priori known its state can be seen as noncorrelated to the navigational state of the vehicle. It then follows that vehicle–landmark covariances in the covariance matrix can be set to zero. The practical meaning of this is that, by forcing the vehicle–landmark covariances to be zero, the vehicle state covariances can be reduced to levels below the initial in the following correction step.

2. Sensor Models

Mathematical models of the measurements taken from the sensors discussed in Sec. II.A are integrated into the above EKF-SLAM framework.

The initial lander 3-DOF navigation state is composed of the position and velocity vectors $\mathcal{R} = [\boldsymbol{p}\ \ \boldsymbol{v}]^\top$. Its update function is based on basic dynamics equations:

$$f(\mathcal{R}, \boldsymbol{u}_{\text{INS}}) = \begin{bmatrix} \boldsymbol{p} + T_s \cdot \boldsymbol{v} + \frac{1}{2} T_s^2 \cdot (\boldsymbol{u}_{\text{INS}} + \boldsymbol{a}_{\text{grav}}) \\ \boldsymbol{v} + T_s \cdot (\boldsymbol{u}_{\text{INS}} + \boldsymbol{a}_{\text{grav}}) \end{bmatrix} \tag{1}$$

where $\boldsymbol{u}_{\text{INS}}$ is the acceleration measured by the INS accelerometer, $\boldsymbol{a}_{\text{grav}}$ is the gravitational acceleration given by the gravity model, and T_s is the update time step (here the accelerometer sampling time step). The accelerations applied to the lander by the thrusters $\boldsymbol{a}_{\text{thrust}}$ are measured by the INS, adding the related process noise ν_{INS}.

$$\boldsymbol{u}_{\text{INS}} = \boldsymbol{a}_{\text{thrust}} + \boldsymbol{\nu}_{\text{INS}} \tag{2}$$

The gravity acceleration additionally applied to the dynamic model is assumed to be perfectly known and the thrust accelerations are assumed to be actuator-noise-free.

For the camera sensors, the following observation model is used comprising the camera projection model as the observation function h_{cam} and the backprojection model as its inverse g_{cam}:

$$h_{\text{cam}}(\mathcal{R}, \boldsymbol{p}_{\mathcal{W},\mathcal{L}}) = \boldsymbol{u} = \boldsymbol{K}\boldsymbol{R}^\top(\boldsymbol{p}_{\mathcal{W},\mathcal{L}} - \boldsymbol{t}) \tag{3}$$

$$g_{\text{cam}}(\mathcal{R}, \boldsymbol{u}) = \boldsymbol{p}_{\mathcal{W},\mathcal{L}} = s\boldsymbol{R}\boldsymbol{K}^{-1}\boldsymbol{u} + \boldsymbol{t} \tag{4}$$

where $\boldsymbol{p}_{\mathcal{W},\mathcal{L}}$ are the coordinates of the observed landmark in the world frame (simple inertial frame centered on plume source); $\boldsymbol{p}_{\mathcal{S},\mathcal{L}}$ are the coordinates of the same landmark in the sensor frame (frame co-aligned with a given sensor); $\boldsymbol{K}$ is the camera projection matrix, projecting a 3D point to 2D camera pixel coordinates; $\boldsymbol{R}$ is the rotation matrix; and $\boldsymbol{t}$ is the translation vector between the two coordinate systems. In cases such as this one, where the sensor does not provide enough degrees of freedom for the function h to be invertible to g, this lacking information is introduced by a further parameter called an inverted prior s representing the distance from the observed 3D point to the camera focal plane.[§§] The pixel measurements of the camera are affected by Gaussian noise with $\boldsymbol{u} = [u \quad v]^\top \sim \mathcal{N}\{\hat{\boldsymbol{u}}, \boldsymbol{U}\}$.[¶¶]

A basic measurement model for the ith beam of a lidar beam bundle is given by transforming the coordinates of the impact point of the lidar beam from the world frame $\boldsymbol{p}_{\mathcal{W},\mathcal{IP},i}$ to the sensor frame $\boldsymbol{p}_{\mathcal{S},\mathcal{IP},i}$.

$$h_{\text{lid},i}(\mathcal{R}, \boldsymbol{p}_{\mathcal{W},\mathcal{IP},i}) = \boldsymbol{R}^\top(\boldsymbol{p}_{\mathcal{W},\mathcal{IP},i} - \boldsymbol{t}) + \boldsymbol{v}_i \tag{5}$$

where similarly to above $\boldsymbol{p}_{\mathcal{W},\mathcal{IP},i}$ are the coordinates of the impact point of beam i in the world frame, $\boldsymbol{p}_{\mathcal{S},\mathcal{IP},i}$ are the coordinates of the same point in the sensor frame, $\boldsymbol{R}$ is the rotation matrix, $\boldsymbol{t}$ is the translation vector between the two coordinate systems, and $\boldsymbol{v}_i$ is a zero-mean Gaussian noise, $\boldsymbol{v} \sim \mathcal{N}\{0, \boldsymbol{R}_i\}$; assuming that the range error and bearing error from a lidar beam are small and uncorrelated, then it can be shown [29] that the covariance matrix for a single ranger measurement is described by

$$\boldsymbol{R}_i = \rho_i^2\sigma_\phi^2\boldsymbol{I} + \left(\frac{\sigma_\rho^2}{\rho_i^2} - \sigma_\phi^2\right)\boldsymbol{p}_{\mathcal{S},\mathcal{IP},i}\boldsymbol{p}_{\mathcal{S},\mathcal{IP},i}^\top \tag{6}$$

where σ_ϕ is the standard deviation of the bearing error (in radians), σ_ρ is the standard deviation of the range error, ρ_i, is the range from the sensor to the laser beam impact point, and $\boldsymbol{I}$ is a diagonal unit 3×3 matrix.

3. Implementation of Landing Navigation

The optical and thermal environments can be sensed using the corresponding camera type. Strongly identifiable points (or features) in the resulting 2D images (e.g., corners, local intensity maxima) can be uniquely associated to particular landmarks in 3D space (feature detection). A matched feature can then serve as the camera measurement in the above EKF-SLAM formulation, to help navigate the lander and localize the observed landmark itself (Fig. 2, above). Thermal cameras can sense in addition local sources of heat, such as the plume sources. Detected features can be a priori known (absolute navigation), or a priori unknown (relative navigation); they can also be detected by either the thermal or the optical camera.

A new so-called hazard frame can be generated from the first lidar measurement. The plume source can also be placed in the same hazard frame by observing it with the thermal camera, assumed to be co-aligned with the lidar. This new lidar frame contains all relevant elements, and landing navigation can be performed in it. This approach is illustrated in Fig. 2 (below) and can be viewed as a SLAM variant of hazard relative navigation often used in safe and accurate landing concepts (e.g., [8]).

C. Hazard Detection and Avoidance

The EnEx Lander must be able to sense and assess terrain hazards and make the autonomous decision to select a new suitable landing site if necessary. A central feature of this approach is the imprecise and uncertain nature of the information coming from the sensors due to environmental, sensor design, and other uncertainties.

[‡‡]Notes on notation when discussing navigation: in this work x denominates a scalar value, $\boldsymbol{x}$ a vector, and $\boldsymbol{X}$ a matrix.

[§§]Introducing an inverted prior to overcome the lack of initialization information for a landmark is not trivial and is discussed in detail in [26,28].

[¶¶]The notation $\boldsymbol{x} \sim \mathcal{N}\{\hat{\boldsymbol{x}}, \boldsymbol{X}\}$ is shortcut for "x is Gaussian with mean $\hat{\boldsymbol{x}}$ and covariance matrix $\boldsymbol{X}$."

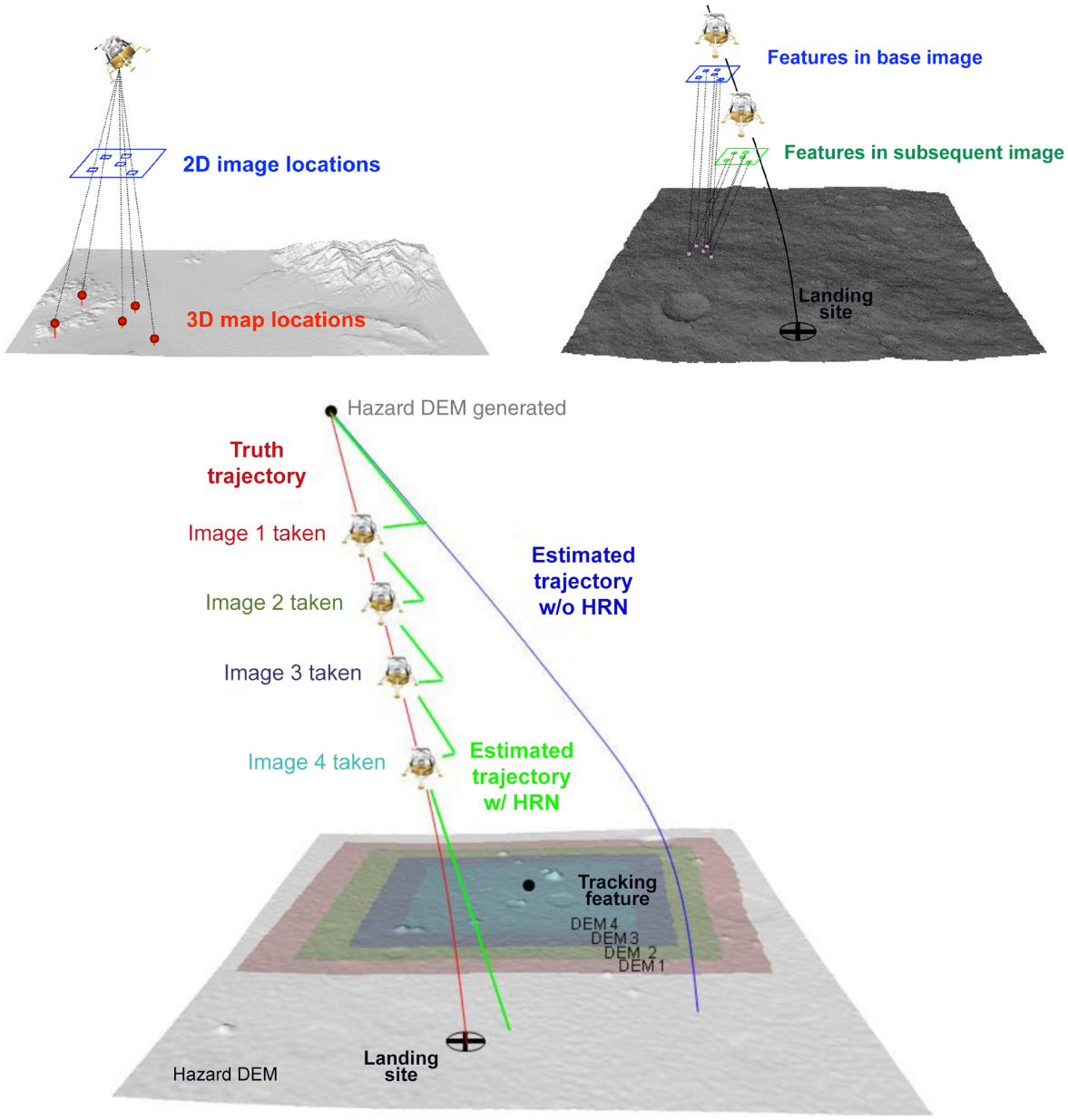

Fig. 2 Above: Correspondences between 2D image-matched features and 3D map locations (left), and between matched features between subsequent images (right) [30]. Below: Hazard relative navigation (HRN) concept [8].

1. Terrain Safety Features

Assuming that the lidar and camera sensors are co-aligned, an enhanced point cloud can be created from the combined illumination, thermal, and point cloud measurements. The enhanced point cloud can then be used as the input to the hazard detection process. Safety feature values and other data for each point in this enhanced point cloud can then be added as further information layers [31].

The lidar point cloud can be used to estimate slope and roughness with least median of squares (LMedSq) regression [31,32]. The local plane parameters a, b, and c at location (x, y) are estimated, and then the slope (θ) is obtained by

$$f_{\theta}^{L}(x,y) = \cos^{-1}\left(\frac{1}{\sqrt{a^2+b^2+1}}\right) \tag{7}$$

The roughness feature r is then the residual of the point cloud and the fitted plane at location (x, y)

$$f_{r}^{L}(x,y) = |d(x,y) - (ax + by + c)| \tag{8}$$

where $d(x, y)$ is the range data from the lidar.

A measure of terrain roughness as observed by the optical camera is obtained by computing the local intensity variance at each pixel [31,32]:

$$f_{r}^{C}(x,y) = \frac{1}{|W|-1}\sum_{i,j\in W}|c(i,j)-\mu|^2 \quad \text{with} \quad \mu = \frac{1}{|W|}\sum_{i,j\in W}c(i,j) \tag{9}$$

where W is a subregion of the camera intensity image $c(x, y)$, $|W|$ is the number of pixels in W, and μ is the mean intensity in subregion W.

Individual obstacle detection from optical camera images can be seen as a clustering or image segmentation problem. The high saliency of either the illuminated faces or the shadows of obstacles in optical images is used to separate the image into obstacle and nonobstacle clusters. In [33], the K-means clustering algorithm is applied to the obstacle detection problem. A Boolean obstacle layer (o) is created for every point on the map:

$$f_{o}^{C}(x,y) = \begin{cases} 1, & \text{for } (x,y) \in O \\ 0, & \text{otherwise} \end{cases} \tag{10}$$

where O is the set of pixel locations in the camera image identified as obstacles.

As mentioned in Sec. II.A, it is assumed that the lidar used is able to sense the texture of the terrain. The Boolean map describing the surface texture as measured by the lidar is given as

$$f_t^L(x,y) = \begin{cases} 1, & \text{for } (x,y) \in S \\ 0, & \text{otherwise} \end{cases} \tag{11}$$

where S is the set of pixel locations in the lidar input identified as snow covered.

The local thermal environment near a plume source can also be leveraged to extract information on the texture of the terrain, by taking advantage of the high differences in thermal inertia, and thus in temperature, between the warmer ice and colder snow on the surface.

To extract explicit texture information from thermal images a two-step process is applied. A background surface temperature distribution is assumed around a plume source, where the location of the plume source, maximum temperature, and Gaussian spread on the surface are considered a priori known. By subtracting this background temperature map from the thermal camera temperature map sensed during landing, a corrected image with pixel values indicating the difference from the local image background is found:

$$T_{\text{corr}}(x,y) = T_{\text{background}}(x,y) - T_{\text{orig}}(x,y) \tag{12}$$

Pixels with negative values in these corrected images will then correspond to warmer temperatures, and thus exposed ice, and positive values should accordingly correspond to snow:

$$f_t^T(x,y) = \begin{cases} 1, & \text{for } T_{\text{corr}}(x,y) \geq 0 \\ 0, & \text{for } T_{\text{corr}}(x,y) < 0 \end{cases} \tag{13}$$

The terrain safety features detectable by each sensor are summarized in Table 1.

A critical parameter is the scientific interest of a map point, here equivalent to the proximity of the point to the plume source. According to the landing requirements, the landing should not be farther away than a given maximum distance $r_{\max}$ from the plume source, but also, for planetary protection reasons, not closer than a minimum $r_{\min}$:

$$r_{\min}^2 \leq (x - x_{PlS,i})^2 + (y - y_{PlS,i})^2 \leq r_{\max}^2 \tag{14}$$

where $(x_{PlS,i}, y_{PlS,i})$ are the coordinates of the ith plume source in the map. Required values for $r_{\min}$ and $r_{\max}$ are 5 and 50 m, respectively (Sec. I).

2. *Fuzzy-Reasoning-Based Landing Terrain Assessment*

Principles of reasoning under uncertainty can be used to first assess landing safety based on terrain features observed by the sensors, and then combine this with information on landing site scientific interest. Different frameworks have gained traction for safe and precise planetary landing applications [31,32,34–36], but due to its simplicity, intuitiveness, and smaller computational requirements, a fuzzy-based landing reasoning approach was chosen for implementation in this work.

Fuzzy inference is the process of formulating the mapping from a given input to an output using fuzzy logic. The input variables, given in crisp numerical values, are first fuzzified (assigned a linguistic label) via the respective membership functions. Using the fuzzified inputs, the fuzzy rules are then evaluated using the logical-fuzzy operands and combined based on the implication method. The combined results are finally defuzzified, giving crisp numerical output values. The process is explained in more detail in [37].

A modified version of the fuzzy approach for landing reasoning given in [35] was applied. Determination of the best landing site is performed in three fuzzy reasoning phases as depicted in Fig. 3.

In the fuzzy safety reasoning step, input from each numeric terrain safety feature is categorized into fuzzy sets. In a fuzzy context, the range of safety scores can be classified into qualitative measures in the form of a linguistic fuzzy set with membership functions of adjacent grades having smooth and overlapping boundaries to avoid abrupt transitions. As an illustrative example for the lidar, the slope was labeled as FLAT for values up to ∼10°, SLOPED from ∼8° to ∼18°, and STEEP from ∼15° on. This gives preference to smaller slopes while respecting the ∼15° slope requirement given in [16].

The fuzzy sets comprise the linguistic labels {HSAFE, MSAFE, MUNSAFE, HUNSAFE}, which stand for highly safe, moderately safe, moderately unsafe, and highly unsafe, respectively. The safety map for each sensor is obtained by applying the appropriate set of rules and membership functions. The detailed membership functions are given in [16]. Fuzzy rules are applied for each sensor as seen in Tables 2 and 3. The sensor hazard linguistic labels in these tables are self-explanatory.

Centroid defuzzification is finally used to produce a numerical safety score s_k for each sensor. The safety score is a weighted combination of the degrees of membership to the fuzzy terrain safety classes

$$s_k(x,y) = \frac{\sum_i p_i A_i}{\sum_i A_i} \tag{15}$$

where $s_k(x,y)$ is the defuzzified terrain safety score for the sensor k (can be either L(idar) or C(amera)[***]) at point (x,y) on the terrain; p_i is the peak value associated with the membership functions; and A_i is the area under the truncated membership function, as calculated during the implication step of the fuzzy assessment (see [37]). The resulting safety score is in the range [0, 10].

The safety scores are then weighted according to the set sensor confidence scores ($\{\beta_L, \beta_C\} \in [0,1]$) and are combined into a single fused safety score according to the equation

$$s_f(x,y) = \frac{\beta_L s_L(x,y) + \beta_C s_C(x,y)}{\beta_L + \beta_C} \tag{16}$$

According to Eq. (14), the landing site must be between a minimum and a maximum distance from the plume source, set at 5 and 50 m, respectively. In the landing reasoning step, a distance weighting function $\beta_d(x,y)$ is introduced to reflect these constraints. The overall landing score of a given map cell is then given by

$$l_{\text{map}}(x,y) = \beta_d(x,y) s_f(x,y) \tag{17}$$

The fuzzy spatial and temporal reasoning step applies a final set of fuzzy reasoning to reflect the fact that the quality of a landing site is connected to the quality of its neighboring sites and does not change over time [35]. The spatial and temporal landing scores (l_s and l_t, respectively) are calculated using a fuzzy assessment process (e.g., if location score is HIGH, and the average of the score of the neighboring locations is LOW, then the spatial score of that location is MEDIUM), and are finally combined using a weighted average to arrive at a final landing score l:

$$l(x,y) = a_s l_s + a_t l_t \tag{18}$$

Table 1 Terrain features that can be detected by each exteroceptive sensor

Sensor	Slope	Roughness	Obstacles	Texture
Lidar	+	+		+
Optical camera		+	+	
Thermal camera				+

***The texture information from the thermal camera is merged with that of the lidar.

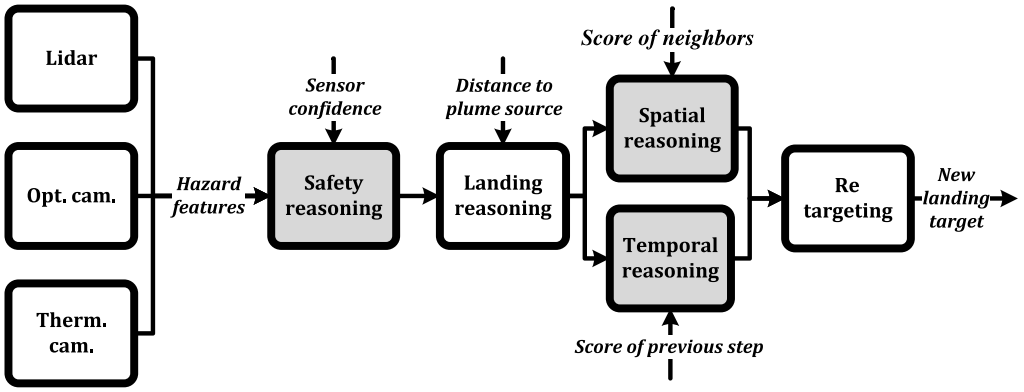

Fig. 3 Block diagram of the selected fuzzy landing site selection approach. Phases where fuzzy reasoning is implemented is shown in gray. Adapted from [35].

Table 2 Lidar safety fuzzy rule set

Texture (prefused)	Operator	Roughness	Operator	Slope	Terrain
SNOW	AND		AND	STEEP	HUNSAFE
SNOW	AND		AND	SLOPED	HUNSAFE
SNOW	AND		AND	FLAT	MSAFE
ICE	AND	VROUGH	OR	STEEP	HUNSAFE
ICE	AND	ROUGH	AND	SLOPED	MUNSAFE
ICE	AND	SMOOTH	AND	SLOPED	MSAFE
ICE	AND	ROUGH	AND	FLAT	MSAFE
ICE	AND	SMOOTH	AND	FLAT	HSAFE

Table 3 Optical camera safety fuzzy rule set

Obstacle	Operator	Roughness	Terrain
PRESENT	and		HUNSAFE
ABSENT	and	VROUGH	HUNSAFE
ABSENT	and	ROUGH	MUNSAFE
ABSENT	and	SMOOTH	MSAFE
ABSENT	and	VSMOOTH	HSAFE

where $a_s + a_t = 1$. The weights can be set equally or can be biased toward either the spatial score or the temporal score. The spatial and temporal rule sets provide a further layer of uncertainty mitigation.

The final landing score l takes into consideration the two key landing factors (terrain safety and scientific interest), as well as spatial and temporal information that further increases the robustness of the assessment. The new optimal site for landing is the point on the terrain with the highest score l, selected only if the score of the currently selected site drops below a preset threshold.

D. Guidance

An extensive survey of guidance laws for safe and accurate planetary landing is performed in [38]. Here, convex guidance optimization is chosen for further implementation, mostly due to its demonstrable optimality, its verifiability, and its operational robustness for real-time application.

Convex guidance was introduced in [39]. The particular implementation investigated here is called Guidance for Fuel Optimal Large Divert (G-FOLD) and is presented in [23,40].

The landing guidance function must calculate the thrust vector profile $\boldsymbol{T}_c$ and trajectory $(\boldsymbol{r}, \dot{\boldsymbol{r}})$ to take the lander from an initial position $\boldsymbol{r}_0$ and velocity $\dot{\boldsymbol{r}}_0$ to a state of rest at the target location on a planetary surface while minimizing fuel use and respecting specific state and control constraints. The general problem is illustrated in Fig. 4.

Because of the minimum throttle requirement for lander engines, the control constraints are not convex; if they could be made so, the problem would be globally optimizable [41]. This issue is resolved in the G-FOLD algorithm by applying "lossless convexification" by using a particular convex relaxation of the control constraints, where a scalar slack variable $\Gamma(t)$ is introduced to lift the control space to a higher dimension and relax the nonconvex set of controls to a convex set. It can be shown that after this introduction the optimal solution to the relaxed problem is always a feasible and optimal solution to the original nonconvex problem [39]. The mathematical foundation behind this finding is described in [39] and the further work cited therein.

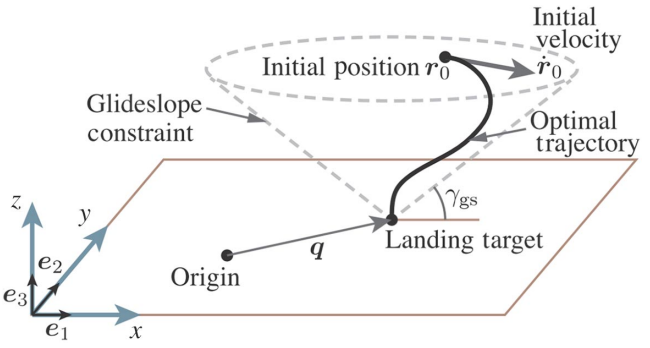

Fig. 4 Illustration of the landing guidance problem (see text for description). Slightly adapted from [23].

The problem with convexified controls is formulated as

$$\max_{t_f, \boldsymbol{T}_c, \Gamma} m(t_f) \tag{19}$$

$$\dot{\boldsymbol{x}}(t) = A\boldsymbol{x}(t) + B\left(\boldsymbol{g} + \frac{\boldsymbol{T}_c(t)}{m}\right), \quad \forall\ t \in [0, t_f] \tag{20}$$

$$\tan\gamma_{gs}\boldsymbol{e}_3^\top \boldsymbol{r}(t) \geq \sqrt{(\boldsymbol{e}_1^\top \boldsymbol{r}(t))^2 (\boldsymbol{e}_2^\top \boldsymbol{r}(t))^2}, \quad \forall\ t \in [0, t_f] \tag{21}$$

$$\|\dot{\boldsymbol{x}}(t)\| \leq \tan(\psi)\|\boldsymbol{x}(t)\|, \quad \forall\ t \in [0, t_f] \tag{22}$$

$$m(0) = m_{\text{wet}} \tag{23}$$

$$\boldsymbol{r}(0) = \boldsymbol{r}_0, \qquad \dot{\boldsymbol{r}}(0) = \dot{\boldsymbol{r}}_0 \tag{24}$$

$$\boldsymbol{r}(t_f) = \boldsymbol{0}, \qquad \dot{\boldsymbol{r}}(t_f) = \boldsymbol{0} \tag{25}$$

$$\dot{m}(t) = -\alpha\Gamma(t), \quad \forall\ t \in [0, t_f] \tag{26}$$

$$\|\boldsymbol{T}_c(t)\| \leq \Gamma(t) \tag{27}$$

$$0 < \rho_1 \leq \Gamma(t) \leq \rho_2 \tag{28}$$

$$\hat{\boldsymbol{n}}^\top \boldsymbol{T}_c(t) \geq \cos\theta\Gamma(t) \tag{29}$$

The optimization objective is expressed in Eq. (19): the lander must expend the minimum amount of propellant, with $m(t)$ being the time-variable lander wet mass (with m_0 the initial lander wet mass), and t_f the time of landing. The dynamics equations for the landing are given in Eq. (20), where $\boldsymbol{x}(t) = (\boldsymbol{r}(t), \dot{\boldsymbol{r}}(t))$,

$$\boldsymbol{A} = \begin{bmatrix} \boldsymbol{0} & \boldsymbol{I} \\ \boldsymbol{0} & \boldsymbol{0} \end{bmatrix} \quad \text{and} \quad \boldsymbol{B} = \begin{bmatrix} \boldsymbol{0} \\ \boldsymbol{I} \end{bmatrix} \tag{30}$$

$\boldsymbol{g}$ is the gravity vector, and $\boldsymbol{T}_c(t)$ is the time variant thrust vector. Equation (26) gives the propellant consumption rate where

$$\alpha = \frac{1}{I_{\text{sp}} g_0} \tag{31}$$

The first state constraint is given in Eq. (21). This equation describes an inverse cone with a slope angle γ_{gs} with its apex on the landing target, within which the lander is allowed to fly. This is termed the "glide slope cone constraint." The unit vectors for each of the axes are noted as $\boldsymbol{e}_{\{1,2,3\}}$ (Fig. 4). The second state constraint in Eq. (22) keeps the velocity magnitude to increasingly lower levels as a function of the lander range-to-target; i.e., the lander is forced to be slower as it nears the target and the surface. This constraint is a line crossing zero in the velocity magnitude versus range space, with a slope of ψ. There are two constraints on the controls: first a thrust magnitude constraint stating a minimum (ρ_1) and a maximum thrust value (ρ_2). Second, Eq. (29) requires that the angle between the thrust vector and the local vertical will not be larger than a given value θ. The two control constraints are convexified and expressed with the help of $\Gamma(t)$.[†††] Equations (23–25) give the initial and final boundary conditions for the optimization problem.

As the fuel cost is a unimodal function of the time of flight t_f, the optimal time of flight can be found with any method for bounded one-dimensional optimization. Its minimum and maximum allowable values are bounded conservatively by the available fuel and maximum throttle [42].

III. Detailed GN&C System and Operations

A detailed baseline system and operations concept can be defined for the approach phase of the landing.

The sensor set is composed of the sensor types described above: an INS, a lidar, an optical, and a thermal camera. Both the optical and thermal cameras have a resolution of 1024×1024, and the lidar has a resolution of 128×128. All sensors have the same angular resolution, and their output is considered perfectly coregistered. A pixel error is assumed for the two cameras, with the thermal camera having a pixel error 2 times higher than that of the optical camera for generic feature detection and 10 times higher for the plume source hot-spot detection, as the thermal camera images are expected to be less sharp than optical ones. For the INS accelerometer, a measurement frequency value of 100 Hz is used and a white noise value is chosen to produce a reasonable drift in lander position as seen in other similar works (1 μg 1σ; see, e.g., [43]). A small generic pointing error of 0.05 deg 1σ was assigned to all exteroceptive sensors. Finally a small multiplicative range error of 0.33% 1σ was assigned to the lidar.

Concerning sensor pointing during landing, an agile approach is required, as each HDA measurement can possibly select a new target landing site. To provide this agility, a solution where the sensor suite is mounted on a gimbaled platform is selected, as has been done for similar platforms for precise and safe landing (e.g., the Morpheus landing testbed [12]). In future studies, a more detailed tradeoff should be performed trading the additional operational flexibility of a gimbaled platform for the lower mass of a fixed platform.

The propulsion system has a maximum thrust-to-weight (TtW) of 5 and a thrust range between 30 and 80% of the nominal maximum. It has an I_{sp} of 220 s.

The start of approach operations, or approach gate (AG), is defined at a range of ~1800 m from the landing target, where lidar is assumed to come in range of the landing area. The velocity at AG was estimated based on a total ΔV for the entire landing of 180 m/s [44]. The uncertainties of the initial conditions for the landing approach phase start were a worst-case combination of values from similar studies [10,43]. The final position- and velocity-required accuracies were at 10 m and 0.25 m/s 3σ, respectively, in all directions. The position uncertainty of the plume source, although in reality would be known with some accuracy before landing start, but still not well enough to satisfy mission requirements, was considered here as practically infinite at start of operations.

Based on the operational considerations for each GN&C function and the operational sequences of similar missions [43,45], a combined concept for the approach phase operations can be given. The operations concept is further illustrated in Fig. 5.

1) Approach Gate to High Gate

a) At AG, the landing site comes in view of the sensors and is within the range of the lidar (~2 km range from the landing site). An optical camera navigation measurement of a priori known points is used for a significant reduction in the lander's navigation state uncertainty.[‡‡‡] Using the improved navigation knowledge, the gimbaled sensor set can be pointed to the nominal landing site.

b) Based on this navigational uncertainty reduction, a new corrective guidance trajectory is calculated, from the newly estimated lander position to the nominal landing site. A large-scale divert maneuver might be necessary depending on the lander position accuracy before AG.

2) HDA High Gate to HDA Low Gate

a) The first HDA measurement is taken at HDA high gate (HG, ~1 km range from landing site).[§§§] An HDA assessment is performed and after it is completed 5 s later [11], a new landing site is possibly selected. A few more (4) HDA measurements are taken at set times so that increasingly higher resolution HDA maps are produced. Each time a new landing site is selected, the sensor set turns on its gimbal to point to the new landing site.

b) From the first lidar measurement, the navigation function can define a new hazard frame. The lander navigation state is then estimated in this new hazard frame. The thermal camera observes the plume source and localizes it on the new hazard frame, based on the EKF-SLAM formulation. As the thermal camera has a wide field of view (FOV), the plume source will be observable for almost the entire landing down to low gate (LG).[¶¶¶]

c) Each time a retargeting is commanded by HDA, guidance calculates a new trajectory to the new landing site. As the overall landing area is less than 100 m across, all diverts are expected to be small and any landing site within this area is assumed to be reachable by the lander.

3) HDA Low Gate to Terminal Gate

a) At HDA LG (~100 m range from landing site), the last HDA measurement is taken, the final retargeting maneuver can take place, and the final guidance trajectory can be calculated.

b) The lander follows the guidance trajectory to terminal gate (TG), where the approach phase terminates with the lander having reached a position of 20 m above a safe target landing site having a navigation state accuracy within the requirements.

[†††] It should be noted here that the important requirement that the final thrust vector of the lander should be pointing upward (representing an upright attitude) was not implemented due to tool-related technical issues. It should be considered in future iterations of this work.

[‡‡‡] Assuming that a priori known landmarks will not be distinguishable at altitudes lower than this due to the low resolution of a priori known maps, this is the only optical absolute navigation measurement.

[§§§] HDA HG is defined as the point at which the first lidar measurement with a meaningful ground resolution for hazard detection can be taken.

[¶¶¶] HDA LG is defined as the point from which the ground area covered by an HDA lidar measurement drops to sizes below the landing footprint.

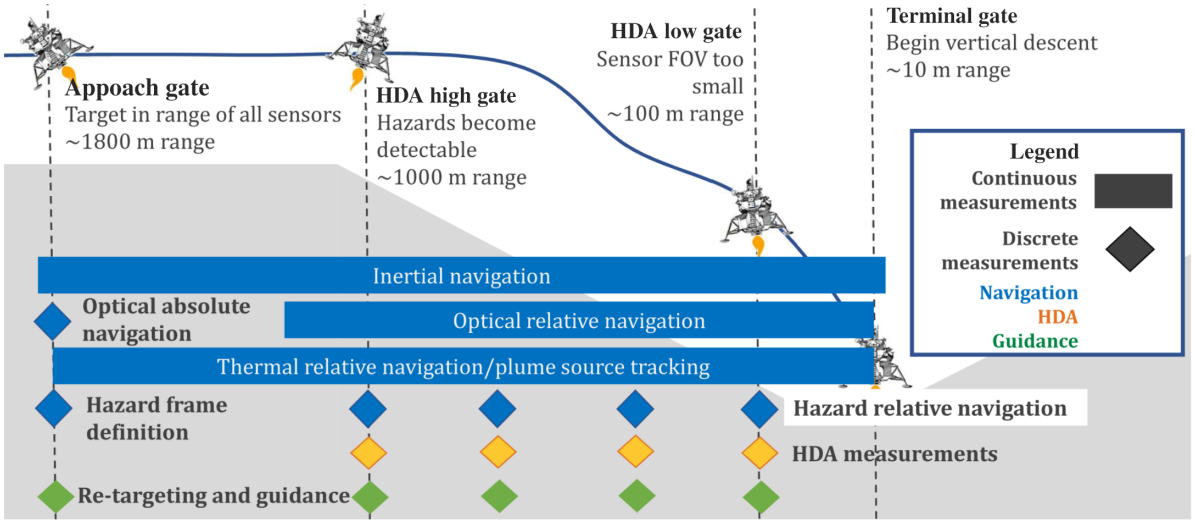

Fig. 5 Baseline concept for landing operations for the EnEx Lander. "Continuous measurements" means measurements with relatively high frequency (~1 Hz) compared with the "discrete measurements" (~0.1 Hz).

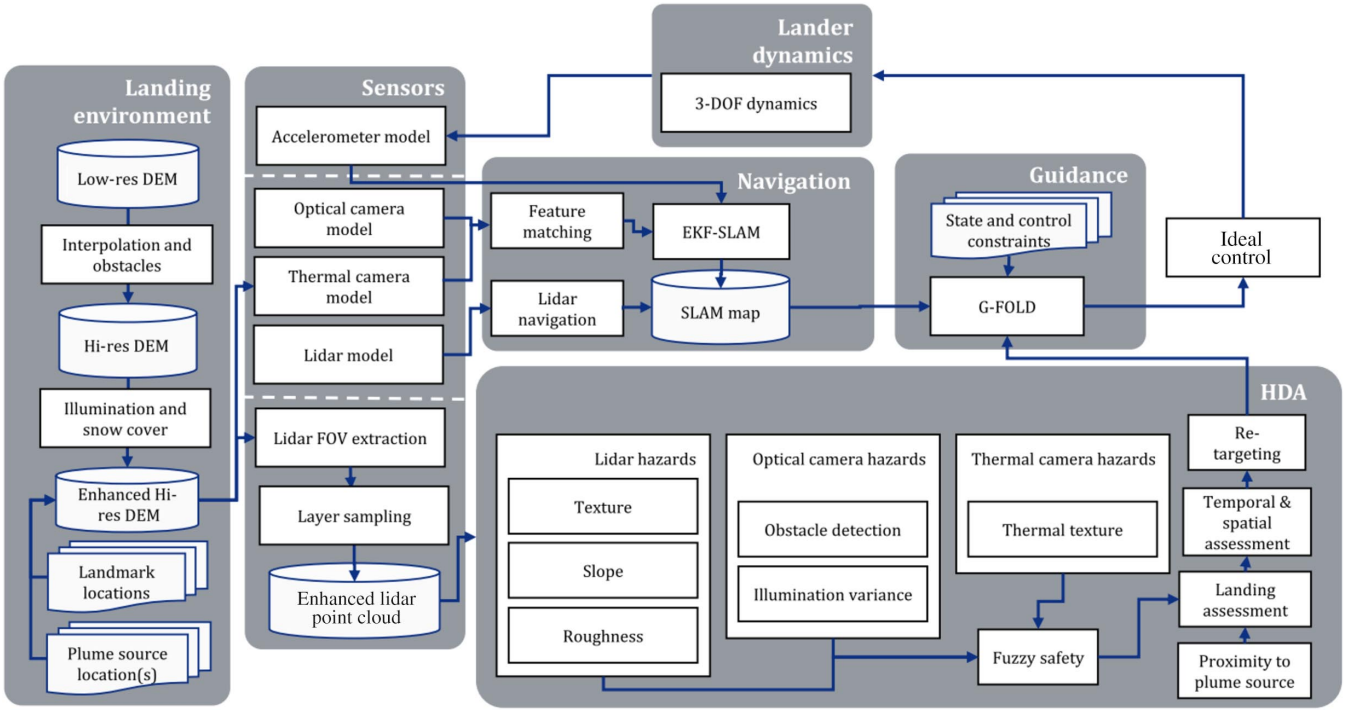

Fig. 6 Architecture of the LandingSim tool, comprising each of the major simulation blocks.

4) Terminal Descent

a) The lander performs the terminal descent, either by free falling to the surface, or by being gently lowered by a sky crane, depending on the design of the mission.

IV. Landing Simulation Tool

A simulation tool called the LandingSim tool was created in MATLAB, implementing the functions described in Sec. II, to assist in analyzing the approach phase GN&C system and operations described above.

The tool comprises several simulation blocks, roughly corresponding to the top-level GN&C functions. The tool architecture is shown in Fig. 6 and is described in detail in [16].

Figure 7 shows the representation of all the relevant elements in the tool. The tool implements a 3-DOF model, with a thrust acceleration vector applied on the point mass lander. Another unit vector represents the pointing direction for all sensors that are assumed to be on a gimbaled platform that can be pointed freely, as discussed above. Each sensor has its own FOV and pixel count. A digital terrain model (DTM) of the landing terrain can be input, in this case a segment of the DTM shown in Fig. 1 (above).[****] The plume source is placed on the DTM, and a higher resolution area is created around it, further populated by obstacles. Sets of both a priori known and a priori unknown optical landmarks are interspersed randomly on the terrain; these points are observed directly by the cameras. Additional illumination, snow, and temperature layers are generated for the terrain. The navigation function also tracks the estimated position of the lander.

****Kindly provided by B. Giese of DLR Cologne.

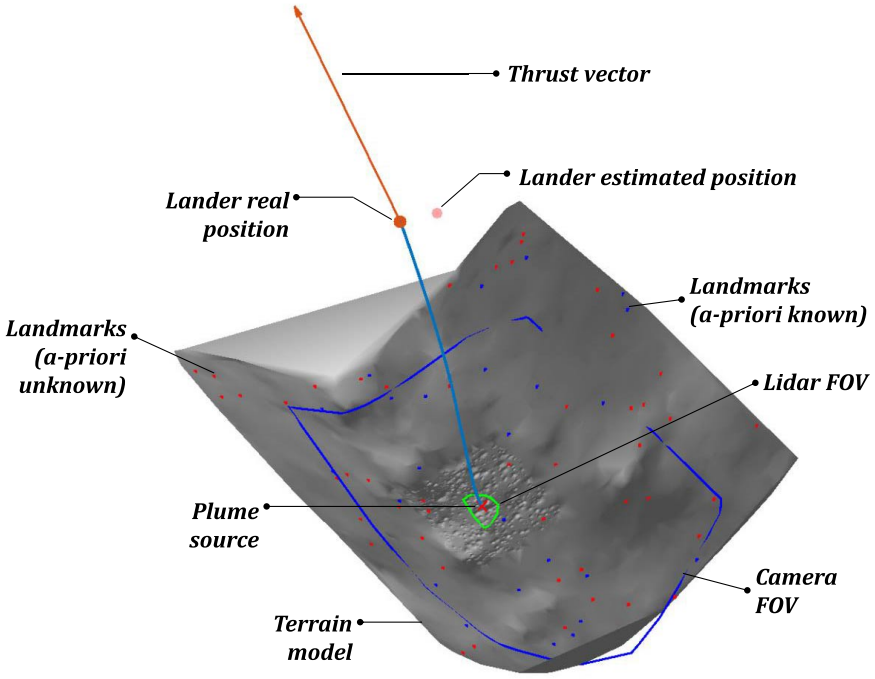

Fig. 7 Illustration of all the relevant entities in the LandingSim tool.

V. Simulation Results

The performance and design results for each of the three central functions are presented in this section. A combined closed-loop simulation is performed thereafter.

A. Navigation Analysis

The navigation function is built on the EKF-SLAM framework (Sec. II.B.1). Each of the elements of the navigation function was validated using Monte Carlo runs and found to be statistically consistent [16]. For each simulation run the navigation error, i.e., the difference between the real navigation state of the lander and that estimated by the navigation function, was tracked. In this section a simple reference trajectory was used (Sec. V.C).

1. *Nominal Performance*

The nominal navigation operations described in Sec. III were simulated. The landing will take place at the height of Enceladan south summer with good illumination conditions for all points of the landing terrain, with only part of the canyon bottom potentially in darkness.

A second scenario was also simulated, taking place in Enceladan polar winter, assuming no illumination. No absolute or relative optical navigation will be possible, possibly even for some time into the braking phase, well before AG. This means that the lander navigation uncertainty will be increased (here estimated by a rough engineering approximation to $\times 2$ of that given in Sec. III). Only the lidar and the thermal camera can then be used for navigation. Because of this, it will be desirable to perform lidar navigation as soon as possible (assumed at a range of $\sim$1800 m) to localize the lander in the hazard frame. Thermal camera relative navigation is used to reduce the uncertainties in velocity.

The simulation results for the two scenarios are presented in Fig. 8. The blue lines in the figure are the magnitudes of the 3σ deviations of lander position, lander velocity, and plume source position, as tracked by EKF-SLAM. Red dotted lines represent the value of the mission requirement for each of these parameters. Both scenarios have similar profiles in all three elements. Initially, a reduction in uncertainty due to the optical absolute navigation measurement takes place in the first scenario and due to the first lidar measurement for the second scenario. The position uncertainties are gradually reduced, mainly due to the contribution of the lidar, and end up within the accuracy requirements. The uncertainties in velocity are more easily and quickly reduced. The uncertainties in the location of the plume source are also slowly reduced down to the required levels. Both scenarios satisfy the landing position and velocity accuracy requirements, with the plume source accuracy requirement marginally satisfied for the first scenario and not satisfied only by a small margin for the second scenario.

An interesting effect is observed in the plume source position uncertainty plot, where the uncertainty remains fixed toward the end of operations. As the plume source for the reference scenario used here is always the pointing target for the sensor set, there is little to no change in the pixel coordinates of the plume source. Its position estimate is therefore not improved and neither is the position uncertainty. In real operations, as the sensor set will be pointed to a target landing site different from the plume source, plume source localization is expected to perform better.

The nominal scenario will be used in all the following analyses. It is improbable, due to several considerations, that landing will be attempted in the darkness of winter. Because of the long duration of winter on Enceladus, however (7–8 Earth years), it would be good to be able to be programmatically flexible.

2. *Sensitivity Analysis*

A sensitivity analysis was performed to determine how system and operational parameters affect the navigation system performance. A host of systems and operational parameters were varied in respect to their nominal values, including sensor ranging and pointing noises, landmarks tracked, initial state uncertainties, and measurement number or frequency.

The magnitudes of the 3σ deviations for lander position and velocity and the plume source position are used in the following as performance metrics. The sensitivity analysis results are given in two types of plots in respect with these metrics (see, e.g., Fig. 9). The varying parameters are given as blue dots on the sensitivity curves. Profile plots show the evolution of the metrics over time for each of these values of the varying parameters, and sensitivity curve plots plot the value of the varying parameters against the final values of the three navigation performance metrics at TG. The sensitivity profiles are plotted in shades of blue, with lighter shades representing higher values of the investigated varying parameter. The respective requirements are represented as dotted red horizontal lines. The fulfillment of requirements at TG is important, but consistent performance

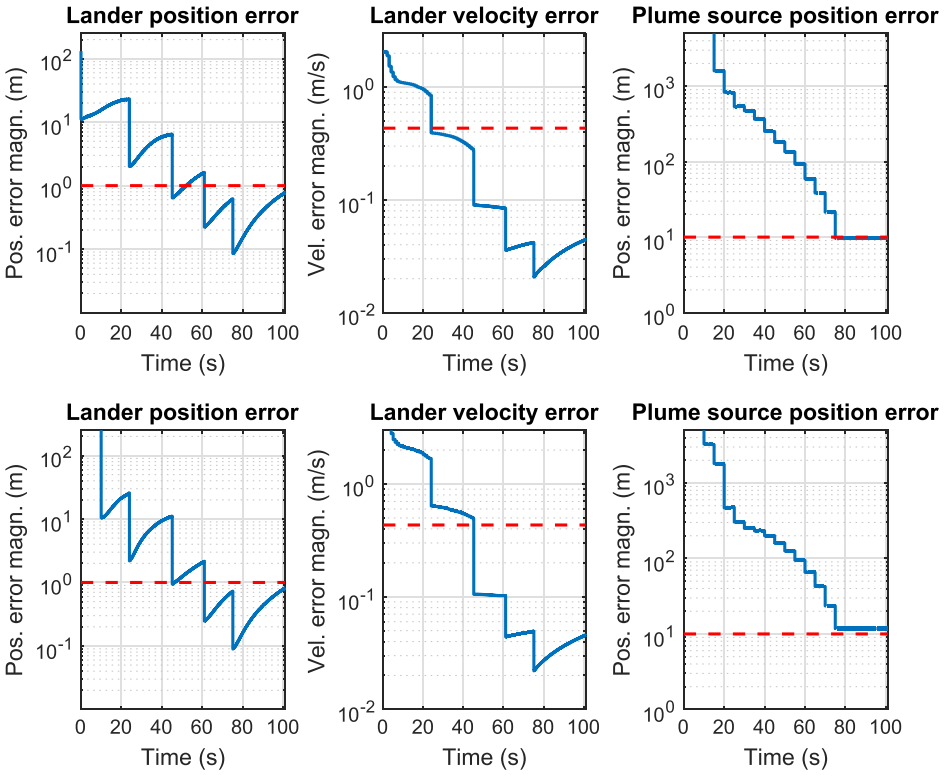

Fig. 8 Navigation performance profiles for the "nominal" (upper) and "landing in darkness" (lower) landing scenarios. See text for description.

during the entire approach phase is beneficial and adds robustness; both sets of plots are therefore indicative of performance.

Here we will discuss the most interesting sensitivity analysis results. A detailed discussion can be found in [16].

Figure 9 shows sensitivity to the number of lidar beams used for navigation. The lidar used here has 128×128 beams, but only some of them are used for navigation purposes to save computational resources. There is significant variation in the profiles throughout the landing for position and velocity. The final position values for small amounts of beam numbers violate the requirements somewhat but not dramatically. A larger number of beams does not increase performance, but would increase robustness in case the return signal of a large percentage of lidar beams would not be detectable. Jumps are observed in the plume source position sensitivity plot attributable

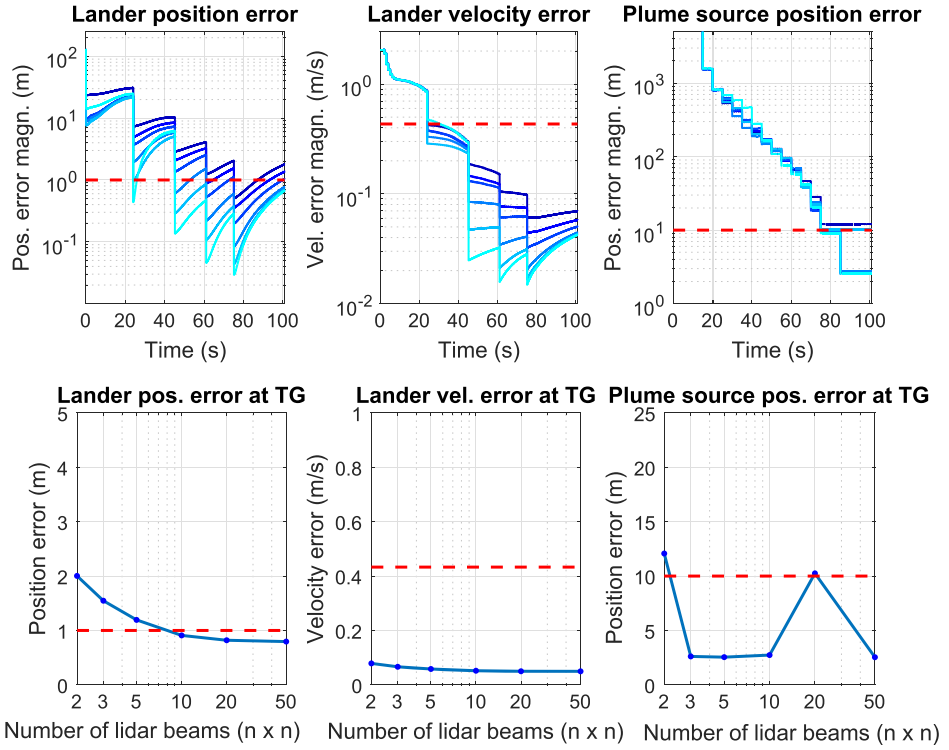

Fig. 9 Lidar beam number sensitivity: performance profiles and sensitivity curves. The blue lines are the 3σ deviations, and the dotted red lines the respective requirements. See text for further explanation.

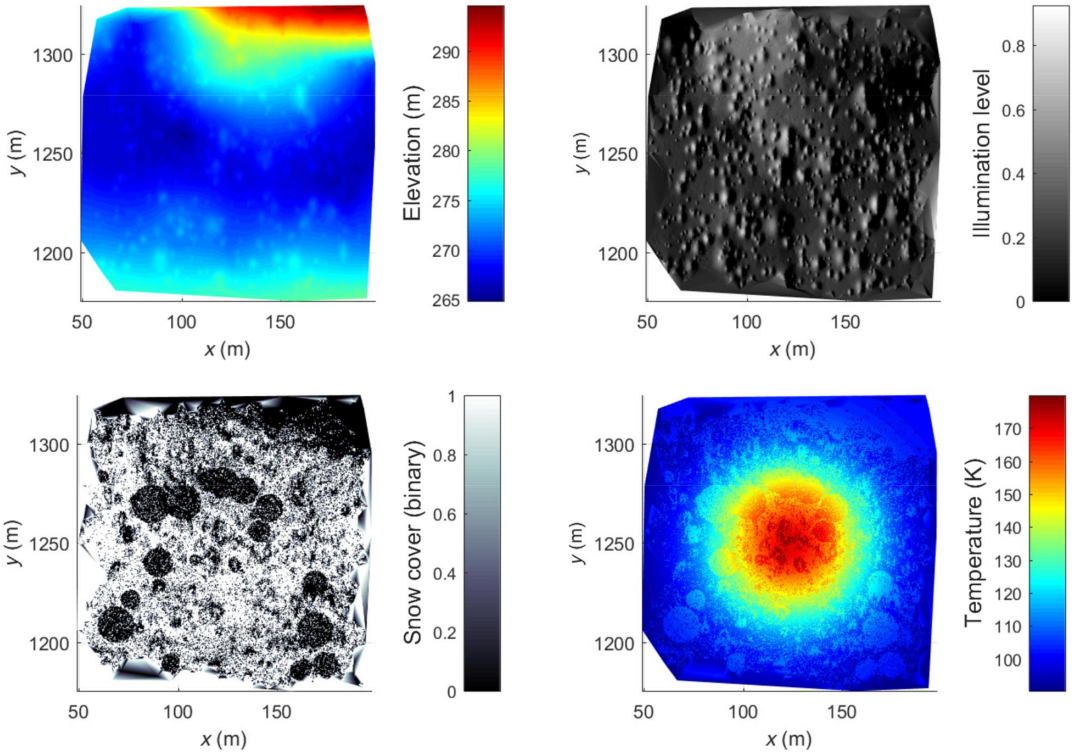

Fig. 10 The input terrain model and its information layers: elevation (upper left), illumination (upper right), snow cover (lower left), and temperature (lower right).

to random effects when sensing the plume source with the thermal camera in the reference scenario used here.[††††]

Considering sensitivity to the number of lidar navigation measurements, a large effect was seen for lander position uncertainty, with less measurements than the nominal significantly violating the requirement, and more measurements than nominal not adding value.

The sensitivity to the frequency of the EKF filter (coinciding in this work with the INS frequency) was also studied. In this work, a relatively high frequency of 100 Hz was used. Similar landing systems, however, use frequencies in the order of 10 Hz (e.g., [12]). Our sensitivity analysis showed that for lower frequencies the accuracy requirements are violated, with the error reaching 2 m for a frequency of 10 Hz. Although this violation is not dramatic, more work is needed in the future to define a concept for inertial navigation with differing INS and filter frequencies and to validate requirements fulfillment for lower filter frequencies closer to those used by the above-mentioned similar landing systems.

A critical parameter was the pointing error of the thermal camera (including the pixel error). It was found to have a dramatic effect on plume source localization, which is logical, as an ability to better pinpoint the feature corresponding to the plume source (hot spot/maximum intensity) means that the plume source landmark will be itself better localized in 3D space. It is expected, however, that hot spots in the camera corresponding to plume sources will not be easy to pinpoint.

A potentially more resource-efficient way to reduce the plume source position uncertainty was found to be by increasing the measurement frequency of the thermal camera for plume source tracking. A higher measurement rate was found to result in significant improvement, even with the original relatively low pixel accuracy of the thermal camera. In particular, increasing the frequency from the original 0.2 Hz to 0.5 Hz significantly improved plume source localization accuracy to levels of ≈1 m. On the contrary, a lower measurement rate resulted in unacceptably high plume source position uncertainty.

Other parameters, such as the performance of absolute and relative optical navigation, initial lander position and velocity uncertainties, and INS measurement frequency, were found to have a small effect on overall performance.

B. HDA Analysis

The Enceladus DTM used for HDA analysis here (Fig. 1, left) had a ground sample distance (GSD)[‡‡‡‡] of ∼100 m. A ∼500 m part of the terrain was chosen, and its resolution was increased as mentioned in Sec. IV. A point representing the plume source was placed in its center, and an area ∼125 m across around it was further refined to a GSD of ∼10 cm.

The illumination, snow cover, and temperature layers of the terrain are shown in Fig. 10. A thousand bell-shaped obstacles of varying sizes (0.2–10 m, uniformly distributed) were randomly distributed on the high-resolution terrain model. Summer illumination conditions were assumed (sun elevation $= 30$ deg, azimuth $= 0$ deg). A probability was assigned that a given face of the DTM is snow covered, based on the local slope. Some circular areas were nonetheless arbitrarily assigned as snow-free. The surface temperature at the plume source was assigned at 180 K and the ambient surface temperature at 100 K. The temperature around the plume source was assumed to follow a 2D Gaussian distribution with $\sigma = 30$ m. Finally, it was assumed that ice surfaces were 10 K warmer than snow-covered ones.

The fuzzy-reasoning-based HDA process was applied on this baseline terrain map. Some of the maps resulting from intermediate steps of the HDA process are shown in Fig. 11. The fused safety maps

[††††]As discussed in Sec. V.A.1, during the final seconds of the reference scenario the lander approaches the plume source hot spot in almost a straight line, with the noisy thermal camera pointing directly to the plume source hot spot. Under these conditions, the plume source position is not well observed and its state is not corrected by the extended Kalman filter. Because of randomness effects, the state of the plume source position is corrected only in some runs during these final seconds. This same effect does not take place in simulations of real operations (Sec. III) as the sensors will not be pointing directly to the plume source, and therefore the pixel value of the hot spot in the thermal camera will be more dynamic and thus better observable during these final seconds of the landing.

[‡‡‡‡]GSD is the distance between pixels, measured on the ground. It represents the resolution of a DTM.

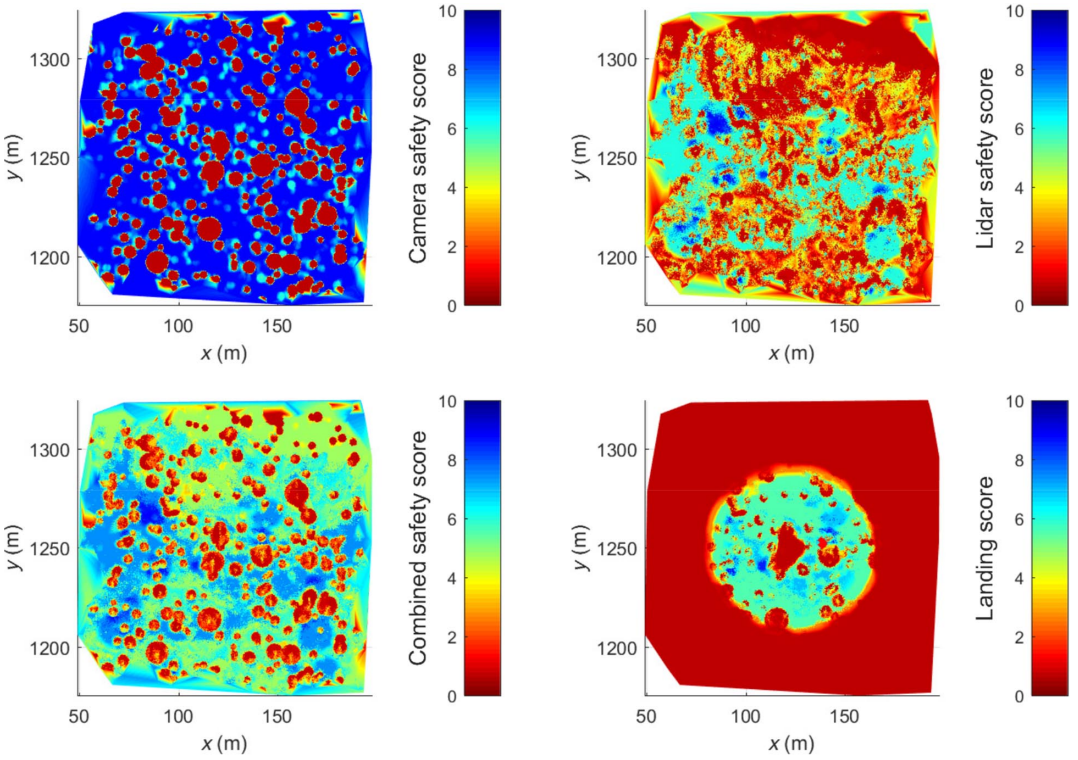

Fig. 11 Maps for some steps of the HDA process: camera safety map (upper left), lidar safety map (upper right), fused safety score for all sensors (lower left), and final landing goodness score (lower right).

combining the safety features for each individual sensor, are shown in the top row. For the optical camera the obstacles are the main source of hazards, with illumination variance coming second. As slope is not being sensed, nonobstacle high-slope areas are given high scores in the optical camera hazard map. For the lidar, the best scoring points are ones that are flat, smooth, and not covered in snow, followed by also smooth and flat but snow-covered points.[§§§§] The fused safety score map for all sensors and the overall landing goodness map (taking distance from the target plume source into account) are then given in the bottom row. The point in the final map with the best landing score is selected as the new landing target (marked as a red *x* in Fig. 11, distinguishable slightly to the right of the center of the map).

To validate the implemented fuzzy-reasoning-based HDA method, the resulting landing safety map (Fig. 11, lower left) was transformed into a safety map with binary safety scores. This was done by setting a threshold score (=6.1) after some calibration. This binary map was then compared with the binary ground truth safety map. The results of this comparison for each point can be any of the three:

False negative (FN): It is a point that is in reality unsuitable for landing and is given as suitable by the HDA process.

False positive (FP): It is a point that is in reality suitable for landing and is given as unsuitable by the HDA process.[¶¶¶¶]

True measurement (TM): The landing suitability of a point is given correctly by the HDA process.

The above FN, FP, and TM can be considered as the HDA performance metrics, as they readily describe the performance of the HDA process in identifying suitable and unsuitable areas for landing.

The validation resulted in significant agreement between the HDA results and the ground truth map (TM = 85%). Eight percent of the map is falsely marked as safe (FN, a potentially dangerous effect), whereas 7% of the map is falsely marked as unsafe (FP, an effect that limits the available area for landing).[*****]

1. *Sensitivity Analysis*

The effects of various system and operational parameters on the goodness of the results of the HDA function were investigated. This was done by comparing the perturbed HDA maps generated from each test run to the original high-resolution HDA map of the test terrain in the previous section. As in the previous section, we will discuss the sensitivity results for the more interesting cases. The full sensitivity analysis is given in [16].

The first sensitivity analysis was in respect to map GSD/resolution. For a given sensor with a certain angular resolution, this value depends only on the range to target that the measurement was taken from.[†††††] A lower-resolution map can also result from the nonnominal case in which some lidar beam return signals are not detected by the lidar head sensor. However, a very large percentage of the return signals have to be missed in order for this to have a noticeable effect in lidar map resolution.

To investigate the dependence of HDA performance on map resolution, the terrain map was down-sampled to various GSD/resolutions. The HDA process was then applied to each of these maps, and the resulting safety map was interpolated. The interpolated map was subtracted from the nominal, high-resolution safety map. This resulted in a new continuous comparison map (in contrast to the binary comparison map in the previous section) with scores ranging from −10 to +10. Negative values on this new comparison map indicate therefore an underestimation of hazardousness by the HDA function, and positive values an overestimation of hazardousness.

[§§§§]Reminder: the lidar hazard map also contains texture information as sensed from the thermal camera and the lidar.

[¶¶¶¶]"In reality" here means the marking of a given point in the ground truth binary suitability map. The terms "positive" and "negative" refer then to hazardousness: an FN therefore falsely gives a negative hazardousness result while an FP falsely gives a positive hazardousness.

[*****]The values for the above performance metrics do not correspond to the likelihood of successful landing, but only represent the agreement between the ground truth and the HDA maps. The successful landing probability is expected to be significantly higher; see Sec. V.B.

[†††††]The effect of the measurement slant angle can be ignored here due to the small FOV of the lidar, and the relatively small slant angles for landing operations.

Accordingly, a given map point is assigned as a true measurement if its score on the comparison map is between −1 and 1, as a false negative if its score is < −1, and as a true positive if its score is >1.

The sensitivity curves for the above resolution analysis are shown in Fig. 12. The comparison map on the right is given for the 2 m GSD case. Redder areas denote increasing hazard underestimation and bluer areas denote increasing hazard overestimation by the HDA function. The trend for smaller resolutions is for the hazard underestimation areas (yellow) to diminish. As expected, larger distances will give a less accurate HDA map. For the nominal resolution of 0.1 m, the TM value is around 80%, and both FN and FP are at around 10%. The values of the performance metrics remain at those levels up to a map GSD of 0.5 m, which is the maximum acceptable obstacle size for the lander. For GSD above this, the HDA process starts missing hazards, and therefore a small increase in FP and dramatic increase in FN are observed.

Next, the sensitivity of the HDA assessment to the input of each of the sensors was investigated, in particular, the case where no optical camera is used for hazard detection, and the case where no texture sensing takes place. As noted before, the optical camera considers all nonobstacle and non-optically-rough areas as highly safe, and thus can give misleading hazard information for these areas. However, with no optical camera input, the redundancy in obstacle detection is lost. In the case where the texture information fused together by the lidar and thermal camera is ignored, the safety of snow-covered areas is overestimated. Depending on the sensitivity of the terminal descent method used and the general lander design to landing on snow, the exclusion of texture sensing might be an acceptable choice to make.

The effect of noise in the elevation of the terrain model points was also investigated. The main source of noise in elevation is lidar range noise. As the noise is multiplicative, measurements taken at larger ranges from target will produce higher elevation noises. In particular, for a lidar range from target at HDA HG of 1100 m, and the nominal multiplicative range noise value of 0.33%, an elevation noise of ∼3.5 m 1σ is given, significantly higher than the size of the minimum acceptable terrain roughness (0.5 m). We see that a 10× reduction in lidar range noise is necessary. In general, a sharp drop in HDA performance was observed when deviating from the ideal, no-noise case.

The sensitivity to errors in the assumed plume source temperature, hot-spot spread, and location was investigated. The effect of a mismatch between the assumed and the real spread of the hot spot around the plume source is that the corrected temperature after subtracting the assumed background temperature is either over- or underestimated, resulting in a ring and lobes of falsely identified texture, with the size of the ring depending on the deviation of the assumed spread from the real one. This results in the false designation of the ring as snow or ice, respectively (Fig. 13, left). A mismatch between the assumed and the real plume temperature will result in the creation of disks around the plume source where texture is falsely estimated as ice for assumed temperatures less than the real, and as snow for assumed temperatures larger than the real (Fig. 13, center). A mismatch in the assumed plume source location results in the formation of two lobes, increasing in size with increasing error, with the lobe pointing to the direction of the location error overestimating snow cover (as it gives higher surface temperatures) and the back lobe underestimating it (Fig. 13, right).

Significant systematic biases in the form of rings and lobes are thus observed from this sensitivity analysis of the thermal hazard detection function. However, the redundancy offered by the lidar texture sensing has a tempering effect on these biases.

2. *Nominal Performance*

After the sensitivity analyses above, nominal values were set for all parameters. The lidar range error had to be reduced to 0.1× the

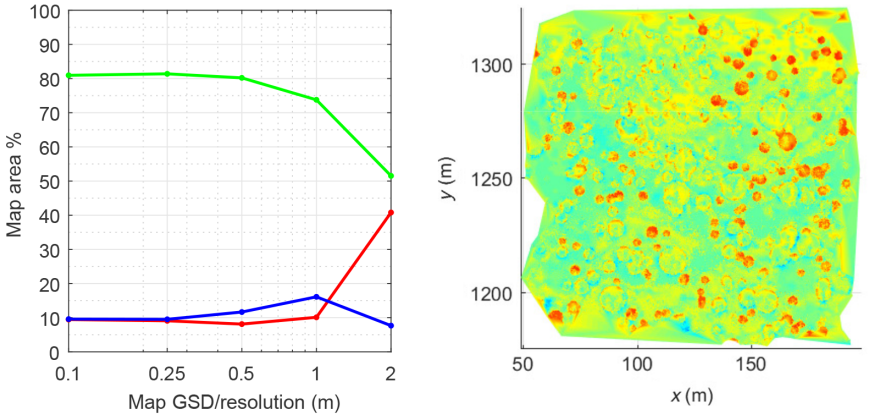

Fig. 12 HDA sensitivity curves for a varying GSD/resolution of the input terrain model (left: green line, TM; red line, FN; blue line, FP). See text for description of comparison map (right).

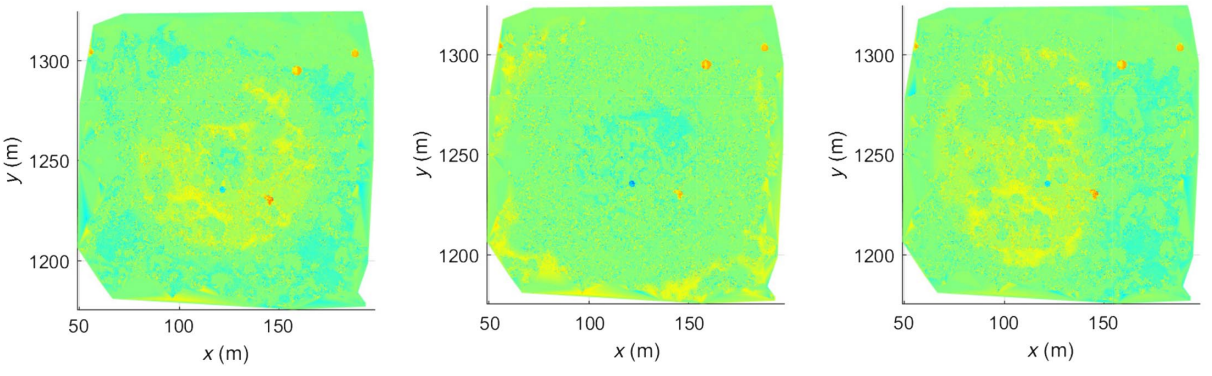

Fig. 13 Comparison maps for errors related to thermal texture sensing (example cases). See text for discussion.

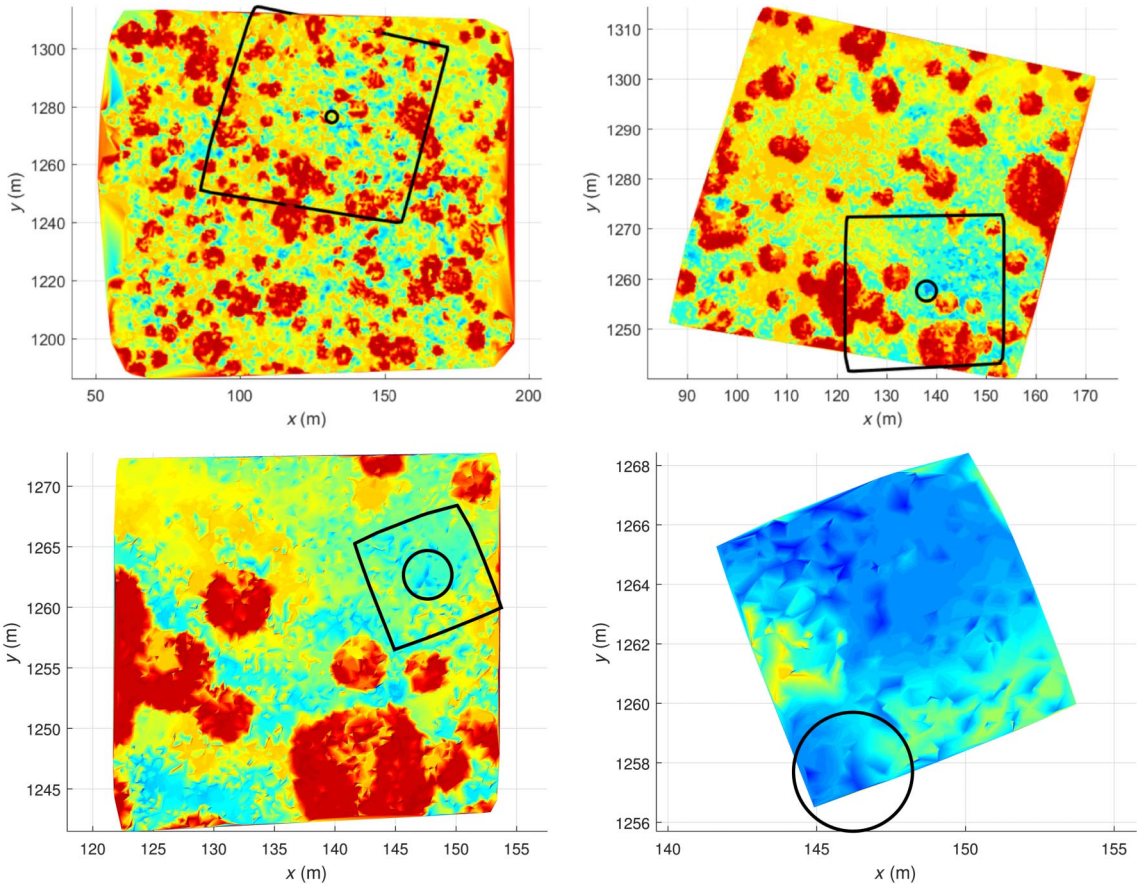

Fig. 14 The four consecutive HDA measurements for the reference landing scenario. See text for details. Color scale is omitted for compactness and is identical to that of Fig. 11.

nominal value so that reasonable roughness values are produced in early measurements.[‡‡‡‡‡] A 10% probability that a lidar beam texture reading would flip was assigned, as well as a 5% probability that the return signal would not be received. Concerning the thermal-camera-related surface temperature assumption errors, a hot-spot spread error of 5 m (1σ), a plume temperature uncertainty of 5 K, and a plume source location uncertainty of 5 m (1σ) were assumed. The nominal landing operations were simulated with the lander following a simple reference landing trajectory (Sec. V.C) while assuming ideal navigation.

Four HDA measurements were made between HDA high and low gate as discussed in Sec. III. The terrain models produced by each of these measurements were processed by the HDA function to produce safety and landing score maps, and to select an new target for landing. The temporal and spatial steps of the HDA process were also applied. This process is illustrated in Fig. 14. Each panel of the figure illustrates the safety map generated by each HDA measurement. On each safety map, a circle represents the lander footprint centered around the new landing target selected by the retargeting function. Finally, a black square illustrates the area within the FOV of the following HDA measurement, centered around the new landing target. As expected, earlier HDA measurements cover a larger area, but produce low safety scores mainly due to the high elevation noise. Scores of the selected target points increasingly grow for each measurement as the lander comes nearer to the surface. The lander footprint increasingly becomes a larger part of an HDA measurement map. A final landing site is chosen in the final HDA measurement.

The evolution of HDA performance throughout landing operations is shown in Fig. 15. As expected for earlier measurements, the FPs generated by false roughness measurements due to high noises in elevation dominate the performance. As the lander gets closer to the sensed surface, the ratio of TMs increases at the expense of FPs, and peaks at about 70%. FNs remain at the same levels throughout operations, at about 10%.

A potentially hazardous scenario emerges, where early low-quality measurements restrain the landing site selection to a low-quality landing area. Operational modifications can be considered for this case, such as taking the first HDA measurement at a lower altitude, or searching for a new target outside the current sensor FOV if there is no point with a score above a given threshold in the current FOV. Each of these solutions comes with their challenges and advantages that should be investigated in the future.

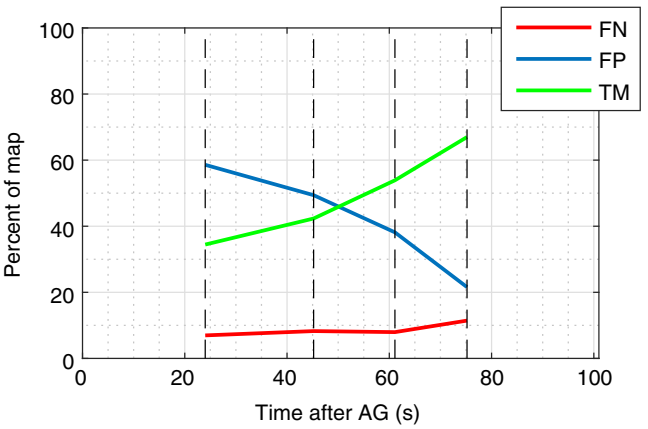

Fig. 15 Evolution of HDA performance throughout the reference landing operations. Time is measured after AG. The times of HDA measurements are marked with dotted vertical lines.

[‡‡‡‡‡]Ways to achieve this reduction (e.g., merging of successive fast lidar measurements) should be investigated in the future.

C. Guidance and Propulsion

The G-FOLD implementation in this work was validated against [41] for a Mars landing scenario [46]. A landing with challenging initial conditions was then simulated to demonstrate the performance of the G-FOLD guidance algorithm.

Figure 16 shows the calculated trajectory and thrust arcs for that scenario, and the projections of that trajectory on the z, y, and x planes, respectively. A smooth trajectory is produced that respects the glideslope constraint (red dotted lines in the projection plots, upper row). The evolution of lander position, velocity, and acceleration acting on the lander are also given on the same figure (middle row). They all evolve smoothly, except for sudden jumps in acceleration when the thrusters are turned to maximum or minimum thrust. Finally, Fig. 16 shows the evolution of the constrained parameters (lower row). The small violations in the velocity and thrust constraints are due to the small relaxation we allowed for, so that the optimizer would converge. This small violation is considered acceptable, also considering the extreme nature of this landing scenario. The lander expends around 60 kg of fuel out 100 kg allocated.

Sensitivity and Worst-Case Analyses

Sensitivity analyses were performed for the guidance function: starting from the nominal initial conditions, the final position, initial position, and velocity direction were varied. No retargeting took place. The results are shown in Fig. 17, for varying final landing site position along and cross range (top), initial lander position along and cross range (middle), and initial lander velocity rotated around the cross range and the altitude axes (bottom). The guidance function can easily deal with highly variable initial and final conditions. The expenditure of propellant varies between ∼45 kg for the close-to-nominal cases and ∼65 kg for the more extreme cases.

Complications emerge, however, when adding retargeting maneuvers, as the fuel-optimal trajectory calculated at the first retargeting will likely have reached the maximum velocity allowed by the velocity magnitude constraint. In subsequent retargetings the guidance function will then lack the ability for large diverts due to this effect.

A two-sided solution to the above problem was devised. First, and as seen by the sensitivity analyses above, the guidance function somewhat overperforms for reachability at AG. A limit can then be set on the available thrust there and slowly relaxed for the following maneuvers. This relaxation was found to be insufficient and a second aspect to the approach was added, the gradual relaxation of the offending velocity magnitude constraint. By setting a relaxation parameter > 0 for the respective constraint inequality in the guidance equations, and gradually increasing it after each maneuver, the necessary flexibility can be achieved by the lander.

To demonstrate and validate this approach a worst-case analysis was performed. The lander was initialized at nominal conditions and a trajectory to the nominal landing site was calculated. At the first retargeting a new target was set at a worst-case distance from the original (2× the ground coverage area [GCA] of the respective HDA

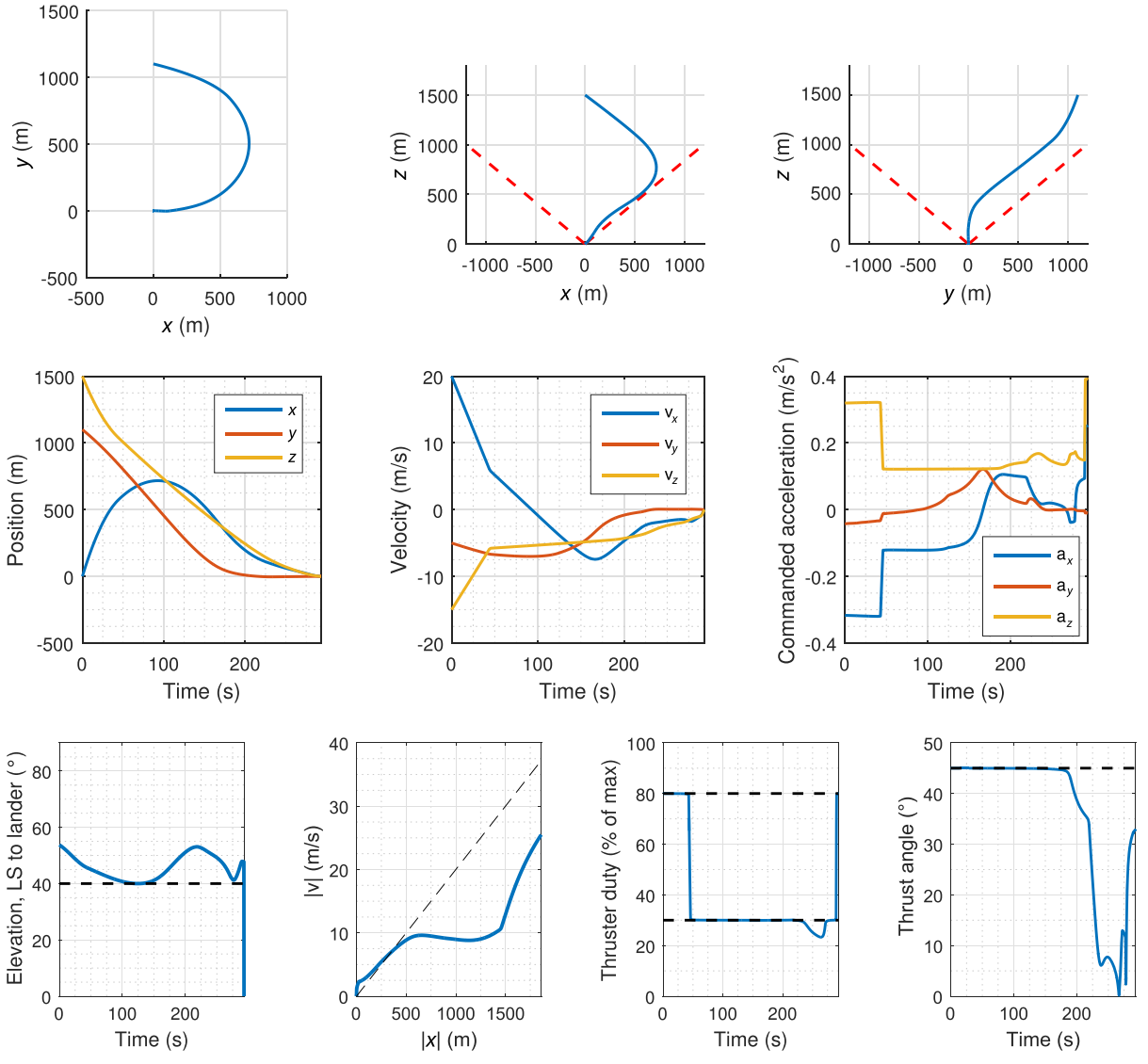

Fig. 16 Demonstration of the trajectory calculated by G-FOLD. Constraints are marked by the black dotted lines (bottom row). See text for discussion.

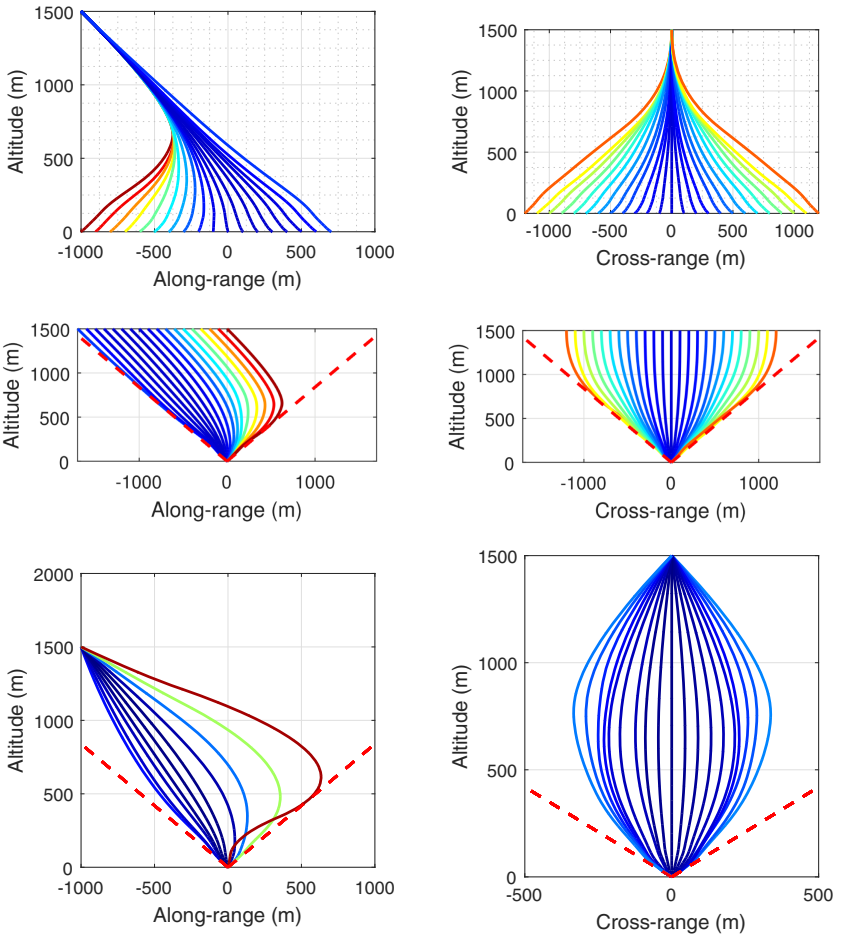

Fig. 17 Sensitivity of guidance at AG to varying initial and final conditions. See text for discussion. Line color corresponds to fuel usage (45 kg [dark blue] to 65 kg [dark red]).

measurement, Fig. 14). This was done for all four retargeting maneuvers, for both the along- and cross-range cases, with each new landing target being moved the appropriate distance to the opposite direction, resulting in a zigzag overall landing trajectory. To allow for the needed increasing guidance flexibility, the thrust upper limit and velocity magnitude were gradually relaxed after each retargeting maneuver.[§§§§§] The results are seen in Figs. 18 and 19. Each target landing site in Fig. 18 has the same color with its respective trajectory segment. Retarget points are marked as blue dots. In Fig. 19, the maximum thrust and velocity magnitude constraints are relaxed after each retargeting command (blue dots) to make the corresponding maneuver possible. The guidance trajectory successfully performs a retargeting at every step. The gradual relaxation of the thrust magnitude and velocity constraints is also visible in the corresponding plots after each retargeting.

D. Combined Simulation Results

To investigate the combined functionality of the LandingSim tool and get a first estimate of landing success statistics, a closed-loop Monte Carlo simulation was performed. In short, for a single Monte Carlo iteration, the lander started from its nominal position, and performed the navigation and HDA functions. Because of technical issues with the solver used for the guidance function in a Monte Carlo environment, as each run required human supervision, it was assumed that whatever target the HDA function commanded was reachable by guidance and with the fuel allocated. This assumption was shown to be reasonable in Sec. V.C. All parameters were noised as indicated by their respective deviation values. System and operations modifications were applied based on some of the discussion from the above analysis. In particular, the thermal camera measurement frequency for navigation was increased from one every 5 s to one every 2 s, the optical camera confidence parameter for HDA was decreased from 1 to 0.2, and the lidar cumulative range noise for HDA was decreased from 0.33 to 0.033%.

One thousand Monte Carlo iterations were performed. Figure 20 demonstrates the fulfillment of navigation requirements and the correct function of the EKF-SLAM machinery. Figure 21 presents the landing success statistics. The overall landing success rate is $P_{\text{Success}} = 94.1\%$. Landing failures are primarily due to landing on high slope terrain, and can be connected to the slightly reduced hazardousness assigned to sloped areas by the optical camera. Obstacles are avoided in almost all cases, and areas with little snow cover are mostly preferred. Seven runs ended within the critical no-go zone around the plume source.

Figure 22 further helps in interpreting the results.[¶¶¶¶¶] Successful landing spots are concentrated around map areas corresponding to the high scoring areas of the HDA safety and landing score maps (Fig. 11). The chosen areas are also largely snow-free (Fig. 10). It is further seen that several failed landing areas are at the edges of obstacles, where the HDA function can produce false negatives of hazardousness.

Overall, the landing success rate is high but still not within the ∼99% success rate typical for landing missions. In addition, the worst-case scenario with significant consequences for planetary protection, with the lander entering the plume source no-go zone, has a probability of ∼1%. Further studies will need to be performed to investigate ways to improve both these metrics.

[§§§§§] The amount of relaxation was manually calibrated. In the future, a more formal and automated way will have to be found.

[¶¶¶¶¶] The cross-range velocity error plot was intentionally cut off at 10^{-2} m/s to maintain plot clarity for the error plots of the velocity components. The error for the cross-range velocity component follows the same behavior below the cutoff and keeps being bounded by the EKF-estimated 3σ covariance.

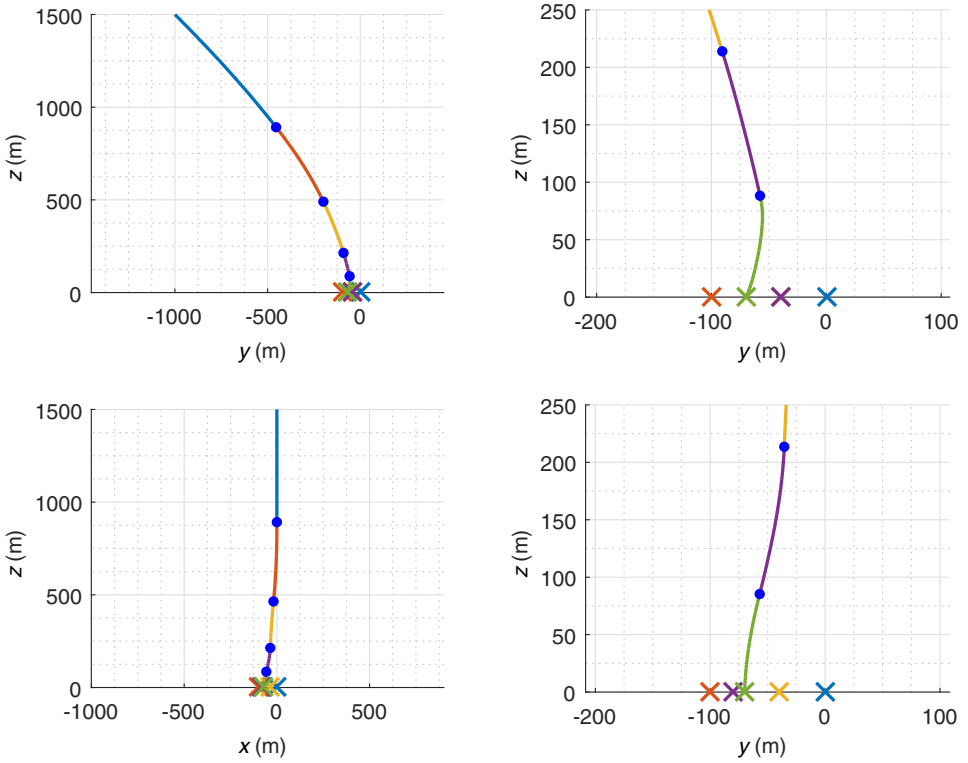

Fig. 18 Zigzagging guidance-calculated worst-case trajectories for the along- (upper) and cross-range (lower) cases, and from a far (left) and near (right) perspective. See text for details.

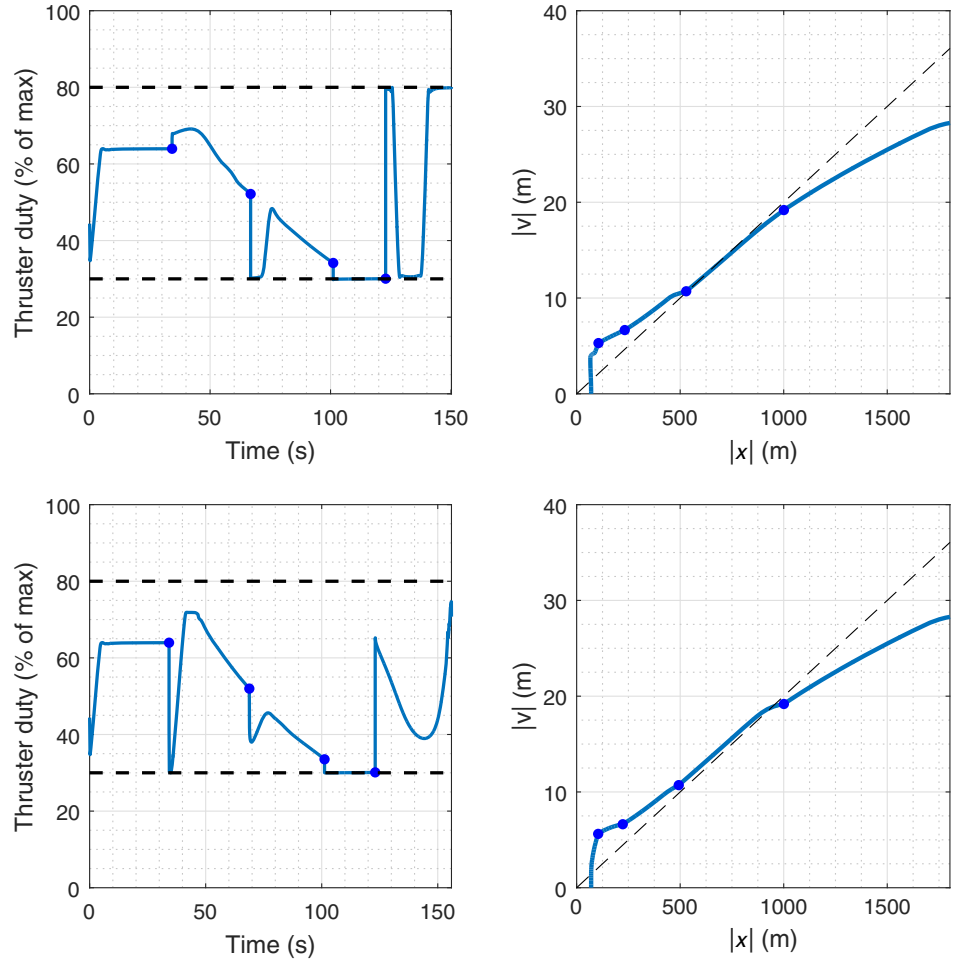

Fig. 19 Thrust duty and velocity versus range to target plots for the worst-case trajectories of Fig. 18. See text for details.

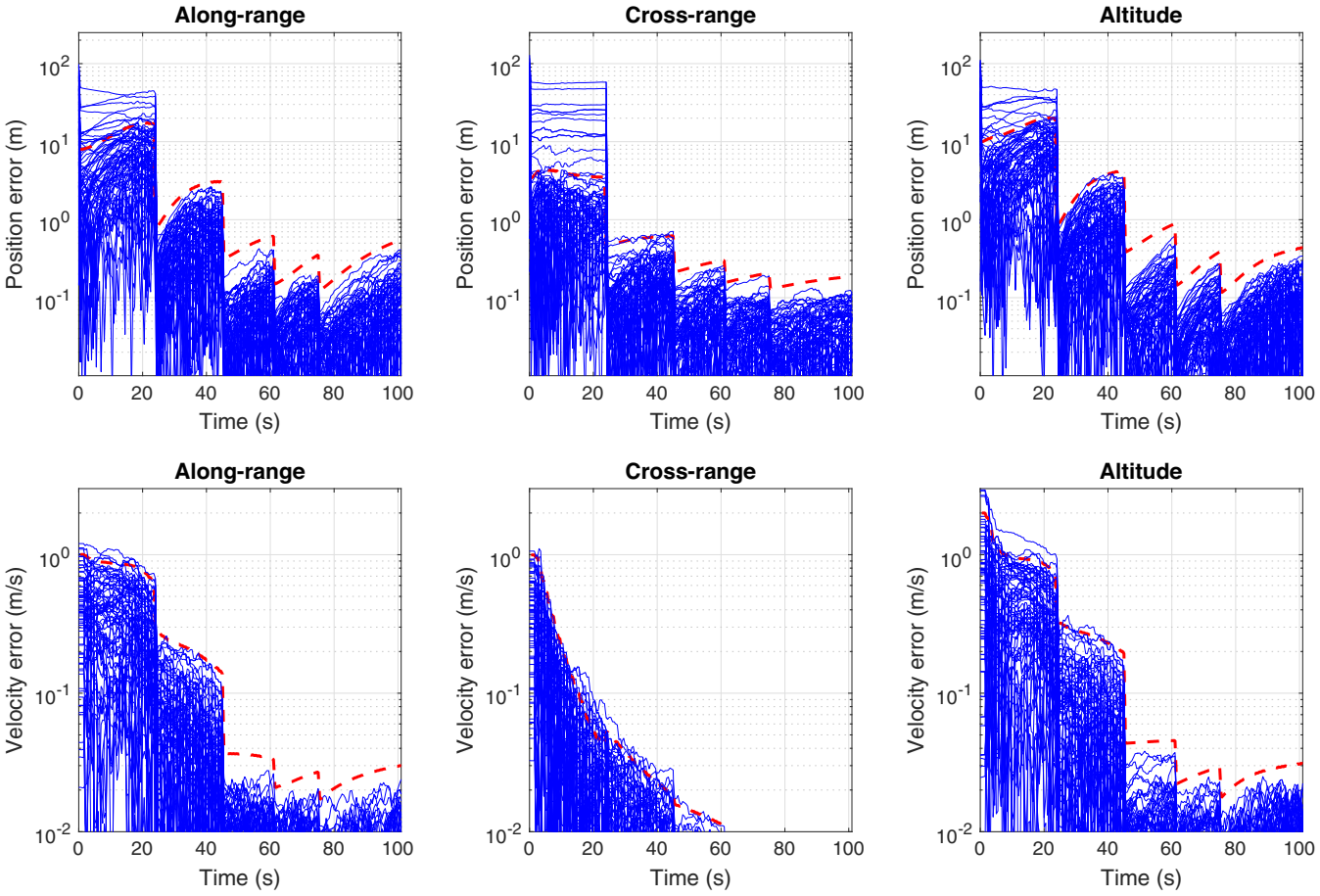

Fig. 20 Monte Carlo run results for the navigation function. The navigation errors are plotted in blue, whereas the 3σ covariances as estimated by the EKF filter are given in red.

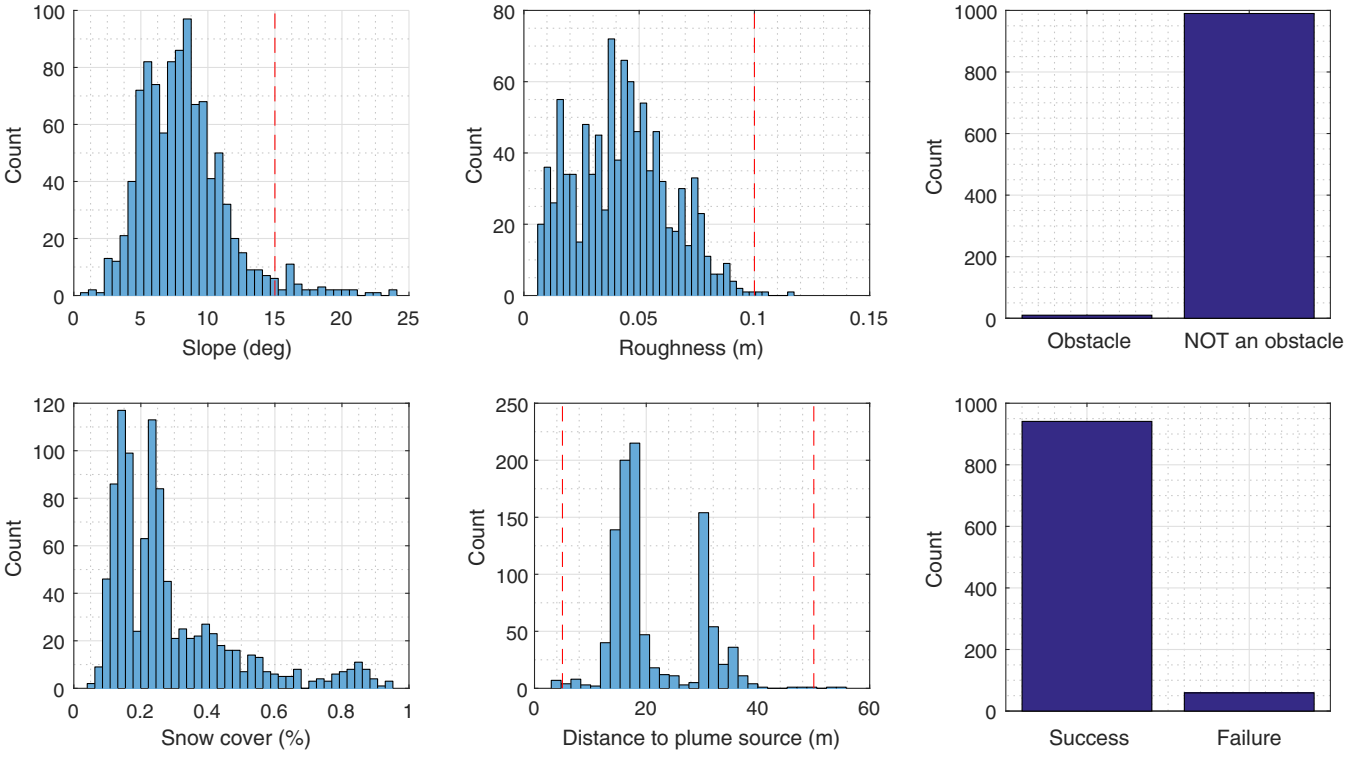

Fig. 21 Distributions of landing success criteria. Requirements are marked with red dotted lines.

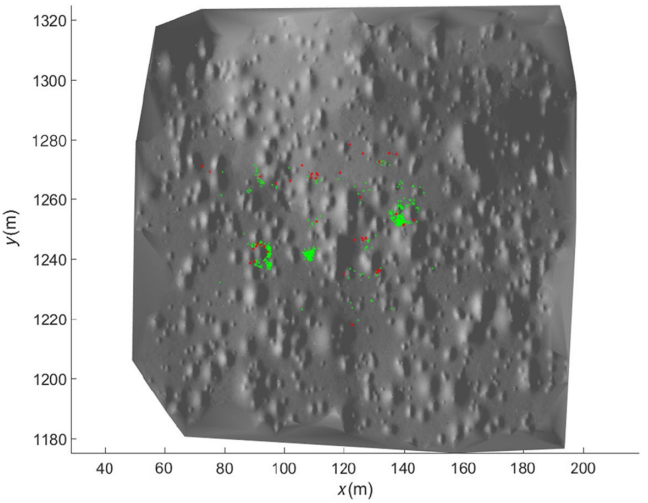

Fig. 22 Final landing sites on the landing terrain. Green dots represent landing success, and red landing failure. Red dots are plotted bigger for better visibility.

VI. Conclusions

Landing near a plume source inside the tiger stripes canyons of Enceladus is uniquely challenging: it involves aspects not encountered by other similarly ambitious mission concepts, including landing in a polar canyon, on a snow-covered terrain with hazardous texture, and on an extremely sensitive area from a planetary protection point of view. The GN&C system for this landing must be extraordinarily capable and reliable. This work takes the first steps toward the creation of this system, in particular for the final critical landing approach phase, where its full capabilities must be deployed.

Novel sensing capabilities were found to be highly beneficial, namely, a lidar that is capable of sensing texture by analyzing the beam return signal and a thermal camera that can be used for navigation and (indirectly) surface texture sensing. For navigation, thermal sensing integrated in a SLAM framework was found to be able to localize a plume source with the required accuracy despite the low pixel accuracy of thermal cameras and the spread of the thermal signature of the plume source. The simple and novel approach developed to extract surface texture information by using thermal images and previous knowledge of the thermal environment is promising but still needs to be made more robust and able to work as stand-alone.

The HDA function is shown to work adequately, successfully combining hazard sensing information from various sensors and other relevant landing information in a fuzzy reasoning framework. The framework's relative informality and requirement for manual configuration can serve as an intuitive introduction in reasoning under uncertainty, but at the same time it can be tedious and difficult to validate. Other methods may be better suited for more complex HDA systems.

For guidance, the G-FOLD convex guidance algorithm implemented is clearly formulated, is robust, and can deal well with multiple constraints. Because of the somewhat conflicting constraints, a more formal robust retargeting constraint relaxation strategy is necessary for the future.

The closed-loop Monte Carlo simulations produce some initial landing success statistics. A 94% landing success rate is achieved, with 1% of the landing cases ending up within the designated no-go zone close to the plume source, which could have negative consequences from a planetary protection point of view. Further refinement is needed to demonstrate a landing success rate of at least the 99% customary to planetary landings.

Future work should expand the studied operations back to de-orbit insertion, add attitude into the conversation by implementing a 6-DOF approach, and add more noises and biases for the sensors and more environmental details.

Acknowledgments

The Enceladus Explorer (EnEx) initiative, funded by the German Aerospace Center (DLR) and the German Federal Ministry for Economic Affairs and Energy (BMWi), formed the basis and served as a starting point for this work [47]. The authors would like to thank several colleagues whose input was invaluable in the development of this work. Graciela Gonzalez Peytavi of Institute for Space Technology and Space Applications (ISTA)–Bundeswehr University offered extensive help on the subject of navigation and Kalman filtering. Dario Izzo of the European Space Agency Advanced Concepts Team provided valuable insights on aspects of the guidance function. The authors also thank Robert Jakob, also of ISTA, for informative discussions in feature detection. Finally, the authors are grateful to the students of Bundeswehr University who contributed to this project with their student theses.

References

[1] Lunine, J. I., "Ocean Worlds Exploration," *Acta Astronautica*, Vol. 131, Feb. 2017, pp. 123–130. https://doi.org/10.1016/j.actaastro.2016.11.017

[2] Parkinson, C. D., Liang, M.-C., Yung, Y. L., and Kirschivnk, J. L., "Habitability of Enceladus: Planetary Conditions for Life," *Origins of Life and Evolution of Biospheres*, Vol. 38, No. 4, 2008, pp. 355–369. https://doi.org/10.1007/s11084-008-9135-4

[3] Chyba, C. F., and Phillips, C. B., "Possible Ecosystems and the Search for Life on Europa," *Proceedings of the National Academy of Sciences*, Vol. 98, No. 3, Jan. 2001, pp. 801–804. https://doi.org/10.1073/pnas.98.3.801

[4] McKay, C. P., Porco, C. C., Altheide, T., Davis, W. L., and Kral, T. A., "The Possible Origin and Persistence of Life on Enceladus and Detection of Biomarkers in the Plume," *Astrobiology*, Vol. 8, No. 5, 2008, pp. 909–919. https://doi.org/10.1089/ast.2008.0265

[5] Porco, C., DiNino, D., and Nimmo, F., "How the Geysers, Tidal Stresses, and Thermal Emission Across the South Polar Terrain of Enceladus Are Related," *Astronomical Journal*, Vol. 148, No. 3, 2014, p. 45. https://doi.org/10.1088/0004-6256/148/3/45

[6] Dachwald, B., Mikucki, J., Tulaczyk, S., Digel, I., Espe, C., Feldmann, M., Francke, G., Kowalski, J., and Xu, C., "IceMole: A Maneuverable Probe for Clean In Situ Analysis and Sampling of Subsurface Ice and Subglacial Aquatic Ecosystems," *Annals of Glaciology*, Vol. 55, No. 65, 2014, pp. 14–22. https://doi.org/10.3189/2014AoG65A004

[7] Konstantinidis, K., Martinez, C. L. F., Dachwald, B., Ohndorf, A., Dykta, P., Bowitz, P., Rudolph, M., Digel, I., Kowalski, J., Voigt, K., and Förstner, R., "A Lander Mission to Probe Subglacial Water on Saturn's Moon Enceladus for Life," *Acta Astronautica*, Vol. 106, Jan. 2015, pp. 63–89. https://doi.org/10.1016/j.actaastro.2014.09.012

[8] Carson, J. M., Restrepo, C., and Villalpando, C., "GN&C Technologies for Safe and Precise Landing," *10th Fault-Tolerant Spaceborne Computing Employing New Technologies*, 2017, https://ntrs.nasa.gov/search.jsp?R=20170004704.

[9] Fisackerly, R., Pradier, A., Gardini, B., Houdou, B., Philippe, C., De Rosa, D., and Carpenter, J., "The ESA Lunar Lander Mission," *AIAA SPACE 2011 Conference & Exposition*, AIAA Paper 2011-7217, 2011.

[10] Zaunick, E., Fischer, D., Ahrns, I., Orlando, G., Polle, B., and Kervendal, E., "Innovative Visual Navigation Solutions for ESA's Lunar Lander Mission," *9th International Planetary Probe Workshop*, CNES, Toulouse, France, 2012, https://websites.isae-supaero.fr/IMG/pdf/zaunick_lunarlander.pdf.

[11] Carson, J. M., Johnson, A. E., Hines, G. D., Johnson, W., Anderson, F. S., Lawrence, S., Lee, D. E., Huertas, A., Amzajerdian, F., Olansen, J. B., Devolites, J., Harris, W. J., Trawny, N., Condon, G. L., and Nguyen, L., "GN&C Subsystem Concept for Safe Precision Landing of the Proposed Lunar MARE Robotic Science Mission," *AIAA Guidance, Navigation, and Control Conference/SciTech Forum*, AIAA Paper 2016-0100, 2016. https://doi.org/10.2514/6.2016-0100

[12] Crain, T. P., Bishop, R. H., Carson, J. M., Trawny, N., Sullivan, J., Christian, J. A., DeMars, K. J., Getchius, J., and Hanak, C., "Approach-Phase Precision Landing with Hazard Relative Navigation: Terrestrial Test Campaign Results of the Morpheus/ALHAT Project," *AIAA Guidance, Navigation, and Control Conference, AIAA SciTech Forum*, AIAA Paper 2016-0099, 2016. https://doi.org/10.2514/6.2016-0099

[13] Carpenter, J., "ESA's Plans for Lunar Exploration, on Behalf of the ESA Lunar Exploration Team Directorate of Human Spaceflight and Oper-

ations," *Annual Meeting of the Lunar Analysis Group*, 2014, https://www.hou.usra.edu/meetings/leag2014/pdf/3019.pdf.

[14] Oberst, J., Hussmann, H., Giese, B., Sohl, F., Shoji, D., Stark, A., Wickhusen, K., and Wählisch, M., "Enceladus (and Europa) Geodetic Framework," *The International Archives of the Photogrammetry, Remote Sensing and Spatial Information Sciences*, Vol. XLII-3/W1, 2017, International Symposium on Planetary Remote Sensing and Mapping, Aug. 2017, https://www.int-arch-photogramm-remote-sens-spatial-inf-sci.net/XLII-3-W1/113/2017/isprs-archives-XLII-3-W1-113-2017.pdf.

[15] Szumski, A., Konstantinidis, K., Förstner, R., and Eissfeller, B., "Enceladus' Environment and the Design of the Enceladus Ice-Probe Navigation System," *AIAA SPACE Forum 2016*, AIAA Paper 2016-5536, 2014. https://doi.org/10.2514/6.2016-5536

[16] Konstantinidis, K., "Holistic Design of a GN&C System for Safe and Precise Autonomous Landing in Very Challenging Planetary Terrains," Ph.D. Thesis, Bundeswehr Univ. Munich, Neubiberg, Germany, May 2019, https://athene-forschung.unibw.de/doc/128251/128251.pdf.

[17] Giese, B., Helfenstein, P., Thomas, P. C., Ingersoll, A. P., Perry, J., Neukum, G., and Porco, C., "The Morphology of an Active Zone near Enceladus' South Pole," *EGU General Assembly*, Vol. 12, Paper :EGU2010-11085, 2010, https://meetingorganizer.copernicus.org/EGU2010/EGU2010-11085.pdf.

[18] Kempf, S., Beckmann, U., and Schmidt, J., "How the Enceladus Dust Plume Feeds Saturn's E Ring," *Icarus*, Vol. 206, No. 2, 2010, pp. 446–457. https://doi.org/10.1016/j.icarus.2009.09.016

[19] Grenstad, S., "Systems Engineering and Environmental Analyses for the Enceladus Lander Mission," Bachelor Thesis, Univ. der Bundeswehr München, Neubiberg, Germany, 2016.

[20] Abramov, O., Raggio, D., Schenk, P. M., and Spencer, J.R., "Temperatures of Vents Within Enceladus' Tiger Stripes," *Lunar and Planetary Science Conference*, Paper 1206, 2015, https://www.hou.usra.edu/meetings/lpsc2015/pdf/1206.pdf.

[21] Calonne, N., Flin, F., Morin, S., Lesaffre, B., Rolland du Roscoat, S., and Geindreau, C., "Numerical and Experimental Investigations of the Effective Thermal Conductivity of Snow," *Geophysical Research Letters*, Vol. 38, No. 3, 2011, Paper L23501. https://doi.org/10.1029/2011GL049234

[22] Degruyter, W., and Manga, M., "Cryoclastic Origin of Particles on the Surface of Enceladus," *Geophysical Research Letters*, Vol. 38, No. 16, 2011, Paper L16201. https://doi.org/10.1029/2011GL048235

[23] Acikmese, B., Aung, M., and Casoliva, J., "Flight Testing of Trajectories Computed by G-FOLD: Fuel Optimal Large Divert Guidance Algorithm for Planetary Landing," American Astronautical Soc. Paper 13-386, San Diego, CA, 2013, pp. 1–14.

[24] Woodman, O. J., "An Introduction to Inertial Navigation," Univ. of Cambridge TR 696, Cambridge, England, U.K., 2007, https://www.cl.cam.ac.uk/techreports/UCAM-CL-TR-696.pdf.

[25] Pirotti, F., "Analysis of Full-Waveform LiDAR Data for Forestry Applications: A Review of Investigations and Methods," *iForest–Biogeosciences and Forestry*, Vol. 4, No. 3, 2011, pp. 100–106. https://doi.org/10.3832/ifor0562-004

[26] Solà-Ortega, J., "Towards Visual Localization, Mapping and Moving Objects Tracking by a Mobile Robot: A Geometric and Probabilistic Approach," Ph.D. Thesis, Lab. d'Analyse et d'Architecture de Systemes du CNRS, Toulouse, France, 2007, http://ethesis.inp-toulouse.fr/archive/00000528/01/sola.pdf.

[27] Solà-Ortega, J., "Simultaneous Localization and Mapping with the Extended Kalman Filter [online database]," 2014, http://www.iri.upc.edu/people/jsola/JoanSola/objectes/curs_SLAM/SLAM2D/SLAM.

[28] Solà-Ortega, J., Vidal-Calleja, T., Civera, J., and Montiel, J. M. M., "Impact of Landmark Parametrization on Monocular EKF-SLAM with Points and Lines," *International Journal on Computer Vision*, Vol. 97, No. 3, 2012, pp. 339–368. https://doi.org/10.1007/s11263-011-0492-5

[29] Sell, J. L., Rhodes, A., Woods, J., and Christian, J. A., "Pose Performance of LIDAR-Based Navigation for Satellite Servicing," *AIAA/AAS Astrodynamics Specialist Conference, AIAA SPACE Forum*, AIAA Paper 2014-4360, 2014. https://doi.org/10.2514/6.2014-4360

[30] Johnson, A., "On-Board Real-Time Techniques for Safe and Precise Landing," *Go for Lunar Landing Conference*, March 2008.

[31] Seraji, H., "A Multisensor Decision Fusion System for Terrain Safety Assessment," *IEEE Transactions on Robotics*, Vol. 25, No. 1, 2009, pp. 99–108. https://doi.org/10.1109/TRO.2008.2006705

[32] Serrano, N., Bajracharya, M., Howard, A., and Seraji, H., "A Novel Tiered Sensor Fusion Approach for Terrain Characterization and Safe Landing Assessment," *2006 IEEE Aerospace Conference*, Inst. of Electrical and Electronics Engineers, New York, 2006, pp. 1–10. https://doi.org/10.1109/AERO.2006.1655795

[33] Huertas, A., Cheng, Y., and Madison, R., "Passive Imaging Based Multi-Cue Hazard Detection for Spacecraft Safe Landing," *2006 IEEE Aerospace Conference*, Inst. of Electrical and Electronics Engineers, New York, 2006, p. 14. https://doi.org/10.1109/AERO.2006.1655794

[34] Serrano, N., "A Bayesian Framework for Landing Site Selection During Autonomous Spacecraft Descent," *2006 IEEE/RSJ International Conference on Intelligent Robots and Systems*, Inst. of Electrical and Electronics Engineers, New York, 2006, pp. 5112–5117. https://doi.org/10.1109/IROS.2006.282603

[35] Serrano, N., and Seraji, H., "Landing Site Selection Using Fuzzy Rule-Based Reasoning," *Proceedings 2007 IEEE International Conference on Robotics and Automation*, Inst. of Electrical and Electronics Engineers, New York, 2007, pp. 4899–4904. https://doi.org/10.1109/ROBOT.2007.364234

[36] Camara, F., Oliveira, J., Hormigo, T., Araujo, J., Ribeiro, R., Falcao, A., Gomes, M., Dubois-Matra, O., and Vijendra, S., "Data Fusion Strategies for Hazard Detection and Safe Site Selection for Planetary and Small Body Landings," *CEAS Space Journal*, Vol. 7, No. 2, 2015, pp. 271–290. https://doi.org/10.1007/s12567-014-0072-y

[37] "Fuzzy Logic Toolbox for Use with MATLAB," User's Guide, Ver. 2, MathWorks, Inc., Natick, MA, 2018, https://www.mathworks.com/help/pdf_doc/fuzzy/fuzzy.pdf.

[38] Gerth, I., and Mooij, E., "Guidance for Autonomous Precision Landing on Atmosphereless Bodies," *AIAA Guidance, Navigation, and Control Conference*, AIAA Paper 2014-0088, Jan. 2014. https://doi.org/10.2514/6.2014-0088

[39] Acikmese, B., and Ploen, S. R., "Convex Programming Approach to Powered Descent Guidance for Mars Landing," *Journal of Guidance, Control, and Dynamics*, Vol. 30, No. 5, 2007, pp. 1353–1366. https://doi.org/10.2514/1.27553

[40] Acikmese, B., and Blackmore, L., "Lossless Convexification of a Class of Non-Convex Optimal Control Problems for Linear Systems," *Proceedings of the 2010 American Control Conference*, 2010, pp. 776–781. https://doi.org/10.1109/ACC.2010.5530931

[41] Blackmore, L., Açikmeşe, B., and Scharf, D. P., "Minimum-Landing-Error Powered-Descent Guidance for Mars Landing Using Convex Optimization," *Journal of Guidance, Control, and Dynamics*, Vol. 33, No. 4, 2010, pp. 1161–1171. https://doi.org/10.2514/1.47202

[42] Bhasin, N. S., Whittaker, W. R., and Atkeson, C. G., "Fuel-Optimal Spacecraft Guidance for Landing in Planetary Pits," Master Thesis, Robotics Inst., Carnegie Mellon Univ., Pittsburgh, PA, 2016, https://ri.cmu.edu/pub_files/2016/4/Fuel-Optimal-Spacecraft-Guidance-for-Landing-in-Planetary-Pits-Neal-Bhasin.pdf.

[43] Ferreira, J., Esteves, D., Seabra, J., and Hormigo, T., "End-to-End GN&C for the Powered Descent and Safe, Precise Lunar Landing," *15th International Planetary Probe Workshop (IPPW-2018)*, https://www.colorado.edu/event/ippw2018/sites/default/files/attached-files/dltech_2_hormigo_presid501_presslides_docid1146.pdf.

[44] Razzaghi, A. I. (ed.), "Enceladus Flagship Mission Concept Study Report," NASA Goddard Space Flight Center, Greenbelt, MD, Aug. 2007.

[45] Lunghi, P., "Hazard Detection and Avoidance Systems for Autonomous Planetary Landing," Ph.D. Thesis, Politecnico di Milano, Milan, 2017, https://www.politesi.polimi.it/bitstream/10589/131168/1/2017-01_PhD_Lunghi.pdf.

[46] Thies, M., "Simulation of Guidance and Hazard Detection and Avoidance for Autonomous Planetary Landing," M.S. Thesis, Inst. for Space Technology and Space Applications (ISTA), Bundeswehr Univ. Munich, Neubiberg, Germany, 2016.

[47] Funke, O., "DLR Explorer Initiatives–Enabling Technologies for Future Robotic Space Exploration," *5th International Planetary Probe Workshop (IPPW-2018)*, 2018, https://www.colorado.edu/event/ippw2018/sites/default/files/attached-files/demotesting_12_funke_presid681_presslides_docid973.pdf.